# Examining molecular determinants underlying heterogeneity of synaptic release probability using optical quantal imaging

Yulia Akbergenova[1,2,3], Yao V. Zhang[1,2,3], Shirley Weiss-Sharabi[1,2,3], Cunningham, Karen L.[1,2], J. Troy Littleton[1,2,3]

[1]The Picower Institute for Learning and Memory, Massachusetts Institute of Technology, Cambridge, United States; [2]Department of Biology, Massachusetts Institute of Technology, Cambridge, United States; [3] Department of Brain and Cognitive Sciences, Massachusetts Institute of Technology, Cambridge, United States;

Correspondence and requests for materials should be addressed to Y.A. (yulakb@mit.edu) or J.T.L. (troy@mit.edu).

The authors declare no competing interests.

## Abstract

Neurons communicate through neurotransmitter release at specialized synaptic regions known as active zones (AZs). Using transgenic biosensors to image postsynaptic glutamate receptor activation following single vesicle fusion events at *Drosophila* neuromuscular junctions, we analyzed release probability ($P_r$) maps for a defined connection with ~300 AZs between synaptic partners. Although $P_r$ was very heterogeneous, it represented a stable and unique feature of each AZ. $P_r$ heterogeneity was not abolished in mutants lacking Synaptotagmin 1, suggesting the AZ itself is likely to harbor a key determinant(s). Indeed, AZ $P_r$ was strongly correlated with presynaptic $Ca^{2+}$ channel density and $Ca^{2+}$ influx at single release sites. In addition, $P_r$ variability was reflected in the postsynaptic compartment, as high $P_r$ AZs displayed a distinct pattern of glutamate receptor clustering. Developmental analysis suggests that high $P_r$ sites emerge from earlier formed AZs, with a temporal maturation in transmission strength occurring over several days.

## Introduction

Synaptic vesicle fusion occurs at specialized regions of the presynaptic membrane known as active zones (AZs). Several evolutionarily conserved structural proteins are enriched in this subdomain of the presynaptic terminal, including RIM, RIM binding protein, Syd-1, Liprin-α, ELKS/CAST/Bruchpilot, Munc13, and Bassoon/Piccolo/Fife (Schoch and Gundelfinger, 2006; Südhof, 2012; Van Vactor and Sigrist, 2017; Zhai and Bellen, 2004). These large macromolecular complexes facilitate clustering of synaptic vesicles and voltage-gated $Ca^{2+}$ channels (VGCCs). The clustering of VGCCs at AZs allow action potential-triggered $Ca^{2+}$ influx to act locally on synaptic vesicles that are docked and primed for release (Acuna et al., 2016; Bucurenciu et al., 2008; Eggermann et al., 2011; Fouquet et al., 2009; Kawasaki et al., 2004). Synaptic vesicle fusion is tightly regulated and occurs through a highly probabilistic process, often with only a small percent of action potentials triggering release from individual AZs (Körber and Kuner, 2016). Although AZs are thought to share the same overall complement of proteins, release probability ($P_r$) for synaptic vesicle fusion is highly variable across different neurons, and even across AZs formed by the same neuron (Atwood and Karunanithi, 2002; Branco and Staras, 2009; Melom et al., 2013; Peled and Isacoff, 2011). Indeed, some AZ-specific proteins are non-uniformly distributed, and the molecular composition of AZs can undergo rapid changes (Glebov et al., 2017; Graf et al., 2009; Liu et al., 2016; Reddy-Alla et al., 2017; Sugie et al., 2015; Tang et al., 2016; Weyhersmüller et al., 2011; Wojtowicz et al., 1994).

The *Drosophila* neuromuscular junction (NMJ) has emerged as a useful system to study release heterogeneity. At this connection, motor neurons form glutamatergic synapses onto bodywall muscles in a stereotypical fashion, with the axon expanding to form ~10-60 synaptic

boutons that each contain many individual AZs (Harris and Littleton, 2015). *Drosophila* AZs are termed T-bars due to their mushroom-like appearance by EM, and contain a similar assortment of proteins to those identified at mammalian AZs (Böhme et al., 2016; Bruckner et al., 2017, 2012; Ehmann et al., 2014; Feeney et al., 1998; Fouquet et al., 2009; Graf et al., 2012; Jan and Jan, 1976; Kaufmann et al., 2002; Kittel et al., 2006; Liu et al., 2011; Owald et al., 2010; Wagh et al., 2006). Each AZ is specifically associated with a postsynaptic glutamate receptor field, usually separated from other PSDs by membrane infoldings that form the subsynaptic reticulum (SSR) (Johansen et al., 1989). Glutamate receptors at the *Drosophila* NMJ are excitatory inotropic non-NMDA receptors that exist as tetramers, with three obligatory subunits encoded by GluRIII, GluRIID and GluRIIE, and a variable 4$^{th}$ subunit encoded by either GluRIIA (A-type) or GluRIIB (B-type) (Featherstone et al., 2005; Marrus et al., 2004; Petersen et al., 1997; Qin et al., 2005; Schuster et al., 1991). GluRIIA containing receptors generate a larger quantal size and display slower receptor desensitization that their GluRIIB counterparts (DiAntonio et al., 1999). The A- and B-subtypes compete for incorporation into the tetramer at individual postsynaptic densities (PSDs) in a developmental and activity-regulated fashion (Chen and Featherstone, 2005; DiAntonio et al., 1999; Marrus and DiAntonio, 2004; Rasse et al., 2005; Schmid et al., 2008).

The stereotypical alignment of individual AZs to distinct postsynaptic glutamate receptor fields in *Drosophila* allowed the generation of genetic tools to optically follow quantal fusion events at single release sites by visualizing glutamate receptor activation (Melom et al., 2013; Peled and Isacoff, 2011). Classically, studies of synaptic transmission have used electrophysiology to measure the postsynaptic effect of neurotransmitter release over a population of release sites (Katz and Miledi, 1969, 1967), precluding an analysis of how

individual AZs respond. By transgenically expressing GCaMP $Ca^{2+}$ sensors that target to the postsynaptic membrane through PDZ binding or myristoylation domains, single vesicle fusion events at each individual AZ can be imaged by following the spatially localized $Ca^{2+}$ influx induced upon glutamate receptor opening. This allows for the generation of $P_r$ maps for both evoked and spontaneous fusion for all AZs formed onto the muscle by the innervating motor neuron (Cho et al., 2015; Melom et al., 2013; Muhammad et al., 2015; Newman et al., 2017; Peled et al., 2014; Peled and Isacoff, 2011; Reddy-Alla et al., 2017). One surprising finding using this quantal imaging approach is that the hundred of AZs formed by a single motor neuron have a heterogeneous distribution of $P_r$, ranging from 0.01 to ~ 0.5, with neighboring AZs often showing greater than 40-fold differences in $P_r$ (Melom et al., 2013; Peled et al., 2014).

Key questions raised by these observations include how $P_r$ is uniquely set for individual AZs, and whether rapid changes in $P_r$ mediate distinct forms of synaptic plasticity. One potential mechanism to explain $P_r$ variability is that presynaptic AZs show distinct $Ca^{2+}$ channel density and subsequent $Ca^{2+}$ influx at single release sites. An alternative model is that $Ca^{2+}$ entry is similar over all AZs, and that evoked $P_r$ is correlated with local cytosolic or synaptic vesicle proteins and their number and/or state (i.e. phosphorylation status). Likewise, another AZ determinant beyond $Ca^{2+}$ channels could be differentially distributed that controls synaptic vesicle docking or priming state. Each of these possibilities could contribute to AZ $P_r$ collectively, or one mechanism might dominate. To gain insight into the molecular mechanisms that control the heterogeneous distribution of $P_r$ at AZs, we employed optical quantal imaging at *Drosophila* NMJs to identify high $P_r$ sites and examine their properties. Our findings indicate that AZs show differential accumulation of $Ca^{2+}$ channels that generate distinct levels of presynaptic $Ca^{2+}$ influx and variable $P_r$, with AZ maturation playing a key role in setting $P_r$.

## Results

### *Drosophila* NMJ synapses display heterogeneity in $P_r$, ranging from functionally silent sites to high $P_r$ AZs

Recent studies have demonstrated that release sites possess unique structural and functional heterogeneity (Éltes et al., 2017; Holderith et al., 2012; Maschi and Klyachko, 2017; Melom et al., 2013; Peled et al., 2014; Reddy-Alla et al., 2017; Sugie et al., 2015). Using the *Drosophila* NMJ, we explored the source of variation in $P_r$ at this synaptic connection. We previously observed that evoked $P_r$ is non-uniform across a population of ~300 AZs formed by motor neuron MN4-Ib onto muscle 4, ranging from 0.01 to ~0.5 in HL3 saline containing 1.3 mM extracellular $Ca^{2+}$ and 20 mM $Mg^{2+}$ (Melom et al., 2013). In our original study, each AZ was defined by ROIs where postsynaptic $Ca^{2+}$ flashes were observed during stimulation, but AZs were not co-labeled in the live preparation. To more closely examine AZ $P_r$ heterogeneity, we identified the position of each corresponding PSD by co-expressing the RFP-tagged glutamate receptor subunit GluRIIA (Rasse et al., 2005). We also created a newer edition of our previous biosensor by generating UAS transgenic animals expressing the $Ca^{2+}$ sensitive GCaMP6s fused with an N-terminal myristoylation (myr) domain. We targeted UAS-myrGCaMP6s to the postsynaptic muscle membrane using Mef2-GAL4 and monitored $Ca^{2+}$ influx after activation of postsynaptic glutamate receptors from spontaneous neurotransmitter release or nerve stimulation (0.3 Hz for 5 minutes) in muscle 4 of early stage 3$^{rd}$ instar larvae (Movie 1). In response to stimulation, synchronous vesicle fusion could be identified across distinct populations of release sites (Figure 1A). During multiple rounds of stimulation, fusion events corresponding to release from different subsets of AZs were observed. However, a small subset of AZs (~10%)

experienced far more frequent fusion events than average, with GCaMP6s activation at the same PSD repeatedly observed during low frequency stimulation (Figure 1A, arrow).

Using this approach, we mapped all myrGCaMP6s visualized release events to the actual position of *in vivo* labeled glutamate receptor PSDs marked by GluRIIA-RFP. Consistent with our previous data, we observed a heterogeneous distribution of AZ $P_r$, with an average $P_r$ of 0.073 ± 0.004 (n = 1933 AZs from 16 NMJs from 16 animals). However, there was a >50-fold difference in $P_r$ between the highest and lowest releasing sites. We plotted the distribution of AZ $P_r$ and observed a skew in the data, with a small number of AZs consistently showing high release rates (75% percentile of $P_r$ was 0.1, with a maximum $P_r$ of 0.73, Figure 1B). Indeed, the release probability data did not fit a normal distribution (D'Agostino $K^2$ test ($p<0.0001$), Shapiro-Wilk test ($p<0.0001$), Kolmogorov-Smirnov test ($p<0.0001$)). Beyond the heterogeneous $P_r$ distribution, 9.7% of all release sites with apposed GluRIIA receptors displayed only spontaneous fusion events, and another 14.6% of the AZ population was silent for both spontaneous and evoked release during the recording period (Figure 1B). In addition, the majority of AZs rarely released a synaptic vesicle following an action potential, with a $P_r$ in the range of 0.01 to 0.2. To functionally examine differences between high and low releasing sites, we categorized all AZs with a release rate greater than 2 standard deviations above average as "high $P_r$", and the remaining AZs that showed evoked release as "low $P_r$". Using these criteria, 65.8% of all AZs fell in the low $P_r$ category with an average release probability of 0.049 ± 0.004. 9.9% of AZs were classified as high $P_r$ sites, with an average release probability of 0.277 ± 0.015 (Figure 1C), indicating high $P_r$ AZs displayed on average a 5.7-fold increased chance of vesicle fusion following an action potential compared to low $P_r$ AZs.

## High $P_r$ AZs correspond to single release sites with enhanced levels of the AZ protein Bruchpilot

One potential caveat to the interpretation of heterogeneous distributions in $P_r$ is the possibility that multiple release sites positioned in proximity to each other contribute to a false identification of high $P_r$ sites. To determine if high $P_r$ sites were due to release from multiple neighboring AZs, we employed high-resolution structured illumination microscopy (SIM) (Figure 1D) and combined it with the quantal imaging method. Presynaptic AZ position can be precisely identified at the NMJ by labeling the core T-bar component Bruchpilot (BRP), the homolog of mammalian ELKS/CAST (Fouquet et al., 2009; Wagh et al., 2006). Using dual color imaging (myrGCaMP6s and GluRIIA-RFP), we first mapped $P_r$ across all AZs, and then fixed the tissue and labeled with anti-BRP antisera. SIM microscopy provides a lateral resolution of labeled biological structures with a limit of ~110 nm (Wegel et al., 2016), allowing separation of individual AZs where the average BRP ring diameter is ~200 nm (Owald et al., 2012). The presence of GluRIIA-RFP allowed precise mapping of release sites between live and fixed tissue, as well as correlation of high $P_r$ sites with SIM labeled BRP-positive AZs (Figure 1D). Using an automated detection algorithm in the Volocity 3D image analysis software, we were able to identify all AZs labeled with BRP (Figure 1D, right panel), and to resolve individual AZ clusters that were not separated using conventional spinning disk microscopy where $P_r$ was determined. The theoretical lateral resolution of the spinning disk confocal microscope for RFP labeled structures is ~280 nm. Analysis of distances between different AZs by SIM indicated that 2.45 ± 0.4% (n = 9 NMJs from 9 animals) of all AZs were located close enough to each other (within 280 nm) such that they would not be resolvable in our live imaging. In contrast, 9.9% (n = 16 NMJs from 16 animals) of AZs were functionally classified as high $P_r$ sites. Therefore, the

174 majority of high releasing sites are not likely to be explained by release events occurring from
175 closely linked AZs.

176 To further analyze single versus closely spaced AZs, release maps were generated where
177 $P_r$ was color-coded to visualize the range of probabilities for all release sites. $P_r$ maps were then
178 compared to BRP-positive AZs identified by SIM. As shown in Figure 1D, the vast majority of
179 high $P_r$ sites were represented by a single BRP-positive AZ that was not further resolvable after
180 SIM imaging (Figure 1D, red circles). These single BRP clusters at high $P_r$ sites were larger and
181 brighter than most other BRP positive puncta (Figure 1E). The average total fluorescence of
182 single BRP puncta from high $P_r$ AZs ($3.95 \times 10^6 \pm 2.67 \times 10^5$, n = 24 AZs from 9 NMJs from 9
183 animals) was 1.7-fold greater than the fluorescence of randomly selected low $P_r$ BRP clusters
184 ($2.33 \times 10^6 \pm 0.98 \times 10^5$, n = 60 AZs from 9 NMJs from 9 animals, $p<0.0001$). To further
185 examine these large single BRP clusters and their release properties, larger clusters that could not
186 be resolved using conventional spinning disk microscopy were separately analyzed. All BRP
187 clusters larger than 280 nm were automatically detected and assigned their release probability
188 parameters measured during live imaging. We then determined whether these sites were
189 represented by single or multiple AZs using SIM microscopy. Clusters > 280 nm in diameter that
190 could be resolved to multiple BRP positive AZs after SIM imaging had a lower $P_r$ ($0.10 \pm 0.02$, n
191 = 35 AZs from 5 NMJs from 5 animals) than those comprised of a single large BRP positive AZ
192 ($0.19 \pm 0.02$, n = 42 AZs from 5 NMJs from 5 animals, Figure 1F). As such, high resolution SIM
193 microscopy confirms that most high $P_r$ sites correspond to single AZs with more intense BRP
194 labeling, consistent with previous data regarding the positive role of BRP in regulating $P_r$ (Peled
195 et al., 2014; Reddy-Alla et al., 2017).

196

## Individual AZ $P_r$ is stable across imaging sessions

We next examined if the non-uniform distribution of $P_r$ across AZs was stable when no plasticity changes were induced. If $P_r$ was highly dynamic at individual AZs over time, unique local synaptic vesicle pools might be an important contributor to the distribution of variable release properties. However, a more stable $P_r$ would argue for a specific factor(s) resident at individual AZs. We were limited in our ability to examine $P_r$ continuously over time intervals greater than 10-15 minutes due to bleaching of GCaMP6s from the high frequency capture rate. Within this constraint, we conducted a 3-minute imaging session using 0.3 Hz stimulation to generate an initial $P_r$ map, and then allowed the preparation to rest for 5 minutes without stimulation or imaging. $P_r$ was then re-mapped in a final 3-minute imaging session using 0.3 Hz stimulation. The activity level of individual AZs was very stable between the two sessions (Figure 2A). This was especially evident for high $P_r$ sites, which sustained high levels of activity during both imaging sessions. Plotting the release rate for all AZs revealed a strong correlation for $P_r$ across the two imaging sessions (Pearson r = 0.77, $R^2$=0.59, p<0.0001, n = 988 AZs from 8 NMJs from 7 animals, Figure 2B). These data suggest that release rate is a unique property of each AZ and is stable over this time interval.

Heterogeneous release rates between AZs might be sensitive to the accumulation of different vesicle populations with variable levels of fusogenicity. If so, a stronger stimulation paradigm that is sufficient to drive vesicle cycling and intermixing would be expected to alter the $P_r$ map. To test this, NMJ preparations were imaged during two low frequency 0.3 Hz stimulation periods separated by a 5-minute 5 Hz stimulation session to induce robust synaptic vesicle turnover and recycling (Figure 2C). Release maps were not dramatically altered by 5 Hz stimulation, with the overall correlation of $P_r$ similar to maps generated without stimulation

(Pearson r = 0.78, $R^2$ = 0.61, p<0.0001, n = 613 AZs from 6 NMJs from 6 animals, Figure 2D). Thus, inducing vesicle recycling with 5 Hz stimulation does not dramatically change $P_r$ across the AZ population, arguing that structural AZ components, versus specific vesicle populations surrounding AZs, are likely to represent the major driver of $P_r$ heterogeneity at this synapse.

## ***Synaptotagmin*** **null mutants display release heterogeneity across AZs**

The synchronous $Ca^{2+}$ sensor Synaptotagmin 1 (Syt1) resides on synaptic vesicles and plays a major role in $P_r$ determination at *Drosophila* NMJs (DiAntonio and Schwarz, 1994; Guan et al., 2017; Lee et al., 2013; Littleton et al., 1994, 1993; Yoshihara et al., 2003; Yoshihara and Littleton, 2002). We hypothesized that if synaptic vesicle proteins play a key role in $P_r$ heterogeneity, in addition to their established role in determining overall $P_r$, then elimination of Syt1 would likely disrupt this heterogeneity. We therefore expressed myrGCaMP6s with Mef2-GAL4 in *syt1* null mutants. As observed electrophysiologically, quantal imaging in *syt1* null mutants revealed a dramatic reduction in evoked release, a shift from synchronous to highly asynchronous fusion, and an increase in spontaneous release rates (Movie 2). To estimate AZ heterogeneity in *syt1* nulls, preparations were stimulated at 5 Hz and release events were normalized to the number of stimuli (Figure 3A). The average release rate per AZ per second in *syt1* nulls during 5 Hz stimulation was 0.03 ± 0.001 (n = 719 AZs from 7 NMJs from 6 animals, Figure 3B). In contrast, spontaneous release rate per AZ in the absence of stimulation was 0.018 ± 0.001 per second in *syt1* nulls (n = 719 AZs from 7 NMJs from 6 animals) compared to 0.011 ± 0.001 in controls (n = 559 AZs from 6 NMJs from 4 animals, p<0.0001, Figure 3B). All visualized release events were mapped to specific AZs and representative $P_r$ heatmaps were

generated (Figure 3A). Although release rate is dramatically reduced in *syt1* nulls, AZs still maintain the overall heterogeneity in $P_r$ distribution across AZs (Figure 3C-E). Comparing the distribution of AZ release rates for *syt1* nulls and controls, release was proportionally decreased across all AZs in *syt1* (Figure 3C). Frequency distribution analysis of AZs with normalized release rates (from 0 to maximum release) confirmed that there was no significant change in the heterogeneity of release between *syt1* mutants and controls (Figure 3D). Likewise, the cumulative frequency distribution of normalized AZ $P_r$ was similar between *syt1* mutants and controls (Figure 3E). Given that AZ release remains highly heterogeneous in the absence of Syt1, these data suggest that variable distribution of key AZ components, rather than heterogeneity of local synaptic vesicle proteins, is likely to control $P_r$ distribution across *Drosophila* NMJ AZs.

## $P_r$ is highly correlated with $Ca^{2+}$ channel abundance at AZs

We next investigated what key AZ protein(s) might control $P_r$. Many structural components of AZs cooperate to regulate positioning of synaptic vesicles in the vicinity of $Ca^{2+}$ channels. Indeed, synaptic vesicle fusion is highly sensitive to $Ca^{2+}$ and most effective in close proximity to $Ca^{2+}$ channels (Augustine et al., 1985; Böhme et al., 2016; Chen et al., 2015; Heidelberger et al., 1994; Katz and Miledi, 1967; Katz, 1969; Keller et al., 2015; Meinrenken et al., 2003, 2002; Stanley, 2016; Wang et al., 2008). As such, $Ca^{2+}$ channel abundance and the subsequent level of $Ca^{2+}$ influx at individual AZs is a compelling variable for $P_r$ heterogeneity. In *Drosophila*, Cacophony (*cac*) encodes the voltage-activated $Ca^{2+}$ channel α1 subunit required for neurotransmitter release (Fouquet et al., 2009; Kawasaki et al., 2004, 2000; Littleton and Ganetzky, 2000; Liu et al., 2011; Rieckhof et al., 2003; Smith et al., 1996). Transgenic animals

expressing fluorescently tagged Cac channels have been previously generated, demonstrating that Cac localizes specifically to AZs at the NMJ (Kawasaki et al., 2004; Matkovic et al., 2013; Yu et al., 2011). To examine the effect of differential Cac distribution on AZ release, dual color imaging experiments were performed where vesicle fusion events were detected by myrGCaMP6s and $Ca^{2+}$ channel distribution was visualized by expression of red-labeled Cac-TdTomato. Preparations were stimulated at 0.3 Hz for 5 minutes and AZ release rate was compared with Cac-TdTomato fluorescence distribution (Figure 4A, B). A strong positive correlation (Pearson r = 0.62, $R^2$ = 0.38, p<0.0001, n = 483 AZs from 7 NMJs from 7 animals) was observed between Cac fluorescence intensity and evoked AZ $P_r$ (representative experiment shown in Figure 4B). We next examined if there was a similar correlation between Cac levels and the frequency of spontaneous vesicle release (minis) at individual AZs. AZ release rates for spontaneous events showed only a mild correlation (Pearson r = 0.19, $R^2$ = 0.04, p<0.0001, n = 483 AZs from 7 NMJs from 7 animals) between mini frequency and Cac density (representative experiment shown in Figure 4C). These results match well with previous observations that release rates for evoked and spontaneous fusion are poorly correlated at *Drosophila* AZs (Melom et al., 2013; Peled et al., 2014), and that spontaneous fusion is largely independent of extracellular $Ca^{2+}$ at this synapse (Jorquera et al., 2012; Lee et al., 2013).

To gain confidence that the observed Cac-TdTomato intensity accurately reflects Cac channel distribution, Cac channels transgenically tagged with GFP were also examined. Postsynaptic expression of myrGCaMP6s obscured Cac-GFP fluorescence, preventing quantal imaging with this sensor in the Cac-GFP background. Therefore, transgenic lines expressing myristoylated red $Ca^{2+}$ indicators previously characterized in the field were generated, including RCaMP1h, R-GECO1 and jRGECO1a. Although RCaMP1h and R-GECO1 were too dim to

visualize localized $Ca^{2+}$ transients at AZs, transgenic lines expressing the myristoylated $Ca^{2+}$ indicator jRGECO1a (Dana et al., 2016) in muscle 4 allowed detection of $Ca^{2+}$ influx events following vesicle fusion at single AZs (Movie 3). In contrast to the more robust GCaMP6s, jRGECO1a has a shorter fluorescent lifetime and the signal amplitude decays more rapidly over time. Indeed, quantal events imaged in transgenic animals expressing myr-jRGECO1a were dimmer and fully bleached within 7-10 minutes of imaging. Therefore, preparations were stimulated at 1 Hz for shorter two minute imaging sessions to generate $P_r$ maps in myr-jRGECO1a expressing larvae (Figure 4D). Using this approach, a strong correlation (Pearson r = 0.54, $R^2 = 0.29$, $p<0.0001$, n = 651 AZs from 7 NMJs from 7 animals) between AZ $P_r$ detected by myr-jRGECO1a and Cac-GFP density was observed (representative experiment shown in Figure 4E). Again, a weaker correlation was found between rates of spontaneous events and Cac-GFP density (Pearson r = 0.17, $R^2 = 0.03$, $p<0.0001$, n = 651 AZs from 6 NMJs from 6 animals). Hence, $P_r$ for action-potential evoked fusion is strongly correlated with the local density of Cac channels at individual AZs, regardless of which fluorophore is used to visualize Cac.

To determine the relative levels of Cac that defined low and high $P_r$ sites, the distribution of Cac-GFP and BRP across the AZ population was examined using SIM microscopy. Similar to the variable levels of BRP described earlier (Figure 1D), variability in the distribution and mean intensity of Cac-GFP fluorescence across AZs at muscle 4 was observed by SIM (Figure 4 – figure supplement 1A, B). 5.72% of AZs displayed Cac-GFP fluorescence greater than 2 standard deviations above average (n = 2011 AZs from 11 NMJs from 3 animals). The mean Cac-GFP fluorescence for these bright AZs (>2 standard deviations above average) was 2.1-fold greater than that observed for the remaining sites ($p<0.0001$, Figure 4 – figure supplement 1C). We next compared Cac-GFP fluorescence obtained for AZs that were functionally classified as

either low or high $P_r$ sites by quantal imaging using myr-jRGECO1a (Figure 4F). The average fluorescence of single Cac-GFP puncta from high $P_r$ AZs (normalized intensity = 0.6 ± 0.04, n = 38 AZs from 7 NMJs from 7 animals) was 2.09-fold greater than the average fluorescence of low $P_r$ AZs (normalized intensity = 0.29 ± 0.01, n = 638 AZs from 7 NMJs from 7 animals, $p<0.0001$). The $P_r$ of AZs classified on the basis of the levels of their Cac-GFP fluorescence was also examined. The average $P_r$ for AZs displaying high Cac-GFP fluorescence (>2 standard deviations above average) was 0.2 ± 0.016 (n = 7 NMJs from 7 animals) compared to 0.06 ± 0.003 (n = 7 NMJs from 7 animals, $p<0.0001$) for the remaining AZs with lower levels of Cac-GFP. Although the absolute number of Cac channels at single AZs is unknown, these data indicate a ~2-fold increase in $Ca^{2+}$ channel number is likely sufficient to change a low $P_r$ site into a high $P_r$ AZ at the *Drosophila* NMJ. Given the steep 3$^{rd}$ to 4$^{th}$ order non-linear dependence of synaptic vesicle fusion with $Ca^{2+}$ (Dodge and Rahamimoff, 1967; Heidelberger et al., 1994; Jan and Jan, 1976), a small change in channel number is likely to have a large effect on $P_r$.

## $P_r$ correlates with the level of presynaptic $Ca^{2+}$ influx measured at individual AZs

Although our data indicate that Cac channel density correlates with AZ $P_r$, a more important functional readout of $Ca^{2+}$ channel activity is the local $Ca^{2+}$ influx occurring at each AZ that drives synaptic vesicle fusion. It is unclear if transgenically tagged $Ca^{2+}$ channel fluorescence intensity functionally reflects a heterogeneous level of $Ca^{2+}$ influx at each AZ. Indeed, $Ca^{2+}$ channels are a source of widespread modulation by second messenger pathways that can alter channel conductivity (Catterall and Few, 2008; Dolphin et al., 1991; Evans and Zamponi, 2006; Reid et al., 2003; Tedford and Zamponi, 2006; Zamponi and Snutch, 1998),

indicating the abundance of $Ca^{2+}$ channels may not be the best proxy for AZ $Ca^{2+}$ entry. In addition, a direct measure of $Ca^{2+}$ influx would be useful to bypass any potential unknown effects on $P_r$ generated by expressing fluorescently tagged Cac. To generate an estimate of the $Ca^{2+}$ influx that each AZ experiences independent of tagging Cac channels, $Ca^{2+}$ influx was visualized by positioning GCaMP6m near $Ca^{2+}$ channels at the AZ. Cac channels cluster in proximity to the AZ structural protein BRP (Fouquet et al., 2009). The C-terminal fragment of BRP is located further away from the AZ, where it spreads into a filamentous "umbrella" like structure. As such, GCaMP6m was added to the N-terminus of BRP, which localizes directly at the base of the AZ where $Ca^{2+}$ channels cluster. Transgenic animals expressing N-terminal GCaMP6m fusions to a BRP fragment (BRP-short) corresponding to amino acids 473–1226 of the full 1740 amino acid protein (Schmid et al., 2008) were generated. BRP-short targets to AZs and co-localizes with native BRP (Fouquet et al., 2009; Schmid et al., 2008). Expression of GCaMP6m labeled BRP-short did not alter its localization, and GCaMP6m fluorescence could be detected presynaptically at individual AZs at 3$^{rd}$ instar larval NMJs (Figure 5A). At rest, N-terminal $^{GCaMP}$BRP-short was dim, consistent with the low levels of resting $Ca^{2+}$ inside terminals (Figure 5A). However, stimulation at 10 Hz resulted in a robust increase in discrete punctated fluorescence that remained confined to single AZs during stimulation (Figure 5A).

To assay the ability of the sensor to detect local $Ca^{2+}$ influx, the stability of $^{GCaMP}$BRP-visualized $Ca^{2+}$ signals during multiple rounds of 5-second 10 Hz stimulation was determined. An image Z-stack was collected from individual boutons, and AZ fluorescence intensity was analyzed for each round of stimulation. Although the amount of fluorescence increase ($\Delta F$) was different for each AZ, it was very stable at the same AZ for each independent stimulation (Figure 5B). AZs that had lower levels of $Ca^{2+}$ influx in the first round of stimulation had similarly low

355 ΔF across all three rounds (Figure 5B). Plotting the frequency distribution of all ΔF signals
356 confirmed that $^{GCaMP}$BRP-short displayed a heterogeneous distribution of ΔF across AZs during
357 stimulation (n = 205 AZs from 6 NMJs from 3 animals, Figure 5C).

358 We next assayed if $Ca^{2+}$ influx detected by $^{GCaMP}$BRP-short is correlated with Cac
359 channel density estimated by the fluorescence of Cac-TdTomato. Animals expressing both
360 transgenes in the presynaptic compartment displayed a strong correlation (Pearson r = 0.73, $R^2$ =
361 0.53, $p<0.0001$, n = 176 AZs from 7 NMJs from 6 animals) between the $Ca^{2+}$ dependent
362 excitation of $^{GCaMP}$BRP-short (ΔF) and Cac-TdTomato intensity at individual AZs during
363 stimulation (Figure 5D, E). In contrast, a weaker correlation (Pearson r = 0.18, $R^2$ = 0.03,
364 $p<0.001$, n = 338 AZs from 8 NMJs from 6 animals) of $^{GCaMP}$BRP-short ΔF and Cac intensity at
365 rest was observed. These data indicate that the overall density of Cac channels detected by
366 fluorescent tagging provides a reasonable estimation of the expected $Ca^{2+}$ influx for each AZ.
367 However, there were some instances where specific AZs experienced a disproportionally low ΔF
368 of $^{GCaMP}$BRP-short signal relative to their Cac-TdTomato intensity (Figure 5D, arrows). This
369 observation suggests that $Ca^{2+}$ influx can be fine-tuned and regulated independently of $Ca^{2+}$
370 channel abundance at certain AZs. As such, measuring both $Ca^{2+}$ channel density and $Ca^{2+}$ influx
371 is likely to provide a more accurate readout of how $P_r$ is controlled by local $Ca^{2+}$ concentrations
372 near the mouth of $Ca^{2+}$ channel clusters.

373 Using $^{GCaMP}$BRP-short as a tool to estimate $Ca^{2+}$ influx at individual AZs, we analyzed
374 the correlation between $^{GCaMP}$BRP-short ΔF induced by 10 Hz stimulation and release rate
375 visualized by myr-jRGECO1a during 1 Hz stimulation at single release sites (Figure 6A, B). AZ
376 heatmaps for both $P_r$ and $Ca^{2+}$ influx fluorescence intensity were generated and compared across
377 the AZ population (Figure 6A). AZs that experienced stronger $Ca^{2+}$ influx displayed the highest

$P_r$ during stimulation. Overall, there was a strong correlation between $Ca^{2+}$ influx and AZ $P_r$ (Pearson r = 0.56, $R^2$ = 0.31, p<0.0001, n = 492 AZs from 6 NMJs from 6 animals, Figure 6B), indicating the levels of $Ca^{2+}$ influx play a major role in determining whether a synaptic vesicle undergoes fusion during an evoked response. In contrast, the frequency of spontaneous vesicle fusion per AZ was only mildly correlated with the amount of $Ca^{2+}$ influx detected by $^{GCaMP}$BRP-short (Pearson r = 0.23, $R^2$ = 0.07, n = 492 AZs from 6 NMJs from 6 animals, representative experiment shown in Figure 6C), consistent with spontaneous release being largely independent of extracellular $Ca^{2+}$ at this synapse. It is worth noting that although a strong correlation between $Ca^{2+}$ influx and evoked $P_r$ was observed at most AZs, a minority population of AZs that displayed robust $Ca^{2+}$ influx had very low $P_r$ (Figure 6B). In summary, these data indicate that $Ca^{2+}$ channel density and $Ca^{2+}$ influx are key factors regulating evoked release at individual AZs. In addition, other factors can negatively influence $P_r$ at a small minority of AZs independent of $Ca^{2+}$ influx.

**Segregation of postsynaptic glutamate receptor subunits at high $P_r$ AZs**

We next examined if glutamate receptor composition in the postsynaptic compartment varied at low $P_r$ versus high $P_r$ AZs. At the *Drosophila* NMJ, glutamate receptors assemble as heteromeric tetramers containing three essential subunits (GluRIII, IID and IIE) and a variable $4^{th}$ subunit of GluRIIA or GluRIIB (Featherstone et al., 2005; Marrus et al., 2004; Petersen et al., 1997; Qin et al., 2005; Schuster et al., 1991). However, it is unclear if GluRIIA and GluRIIB differentially accumulate at AZs in a manner that correlates with presynaptic $P_r$. To visualize GluRIIA and GluRIIB, GluRIIA-RFP and GluRIIB-GFP tagged proteins were expressed under

the control of their endogenous promoters. To image myrGCaMP6s activity without obscuring GluRIIB-GFP, myrGCaMP6s was expressed at low levels using the LexA/LexOP system. We generated LexAop-myrGCaMP6s transgenic animals and expressed myrGCaMP6s in muscle 4 with Mef2-LexA. LexA driven myrGCaMP6s signal is much dimmer than UAS-myrGCaMP6s. The fluorescent signal is observed at very low uniform levels in the muscle membrane in the absence of $Ca^{2+}$ influx, and does not obscure the much brighter GluRIIB-GFP PSD puncta (Figure 7B, middle panel). However, upon $Ca^{2+}$ binding to myrGCaMP6s, the fluorescence dramatically increases at AZs compared to the level of the endogenous GluRIIB-GFP signal, allowing simultaneous imaging of baseline GluRIIB-GFP levels and synaptic activity detected by myrGCaMP6s during stimulation.

Simultaneous expression of GluRIIA-RFP and GluRIIB-GFP revealed a heterogeneous distribution of each subunit across the AZ population, with GluRIIA levels far more variable than GluRIIB (Figure 7A). Indeed, similar to the relatively sparse localization of high $P_r$ AZs across the NMJ (Figure 2), a similar sparse distribution of AZs apposed by very bright GluRIIA PSDs was observed (Figure 7A). To determine if AZs that preferentially accumulate high levels of GluRIIA correspond to high $P_r$ release sites, we mapped $P_r$ across the AZ population in GluRIIA-RFP/GluRIIB-GFP expressing animals. Analysis of the $P_r$ map revealed a strong positive correlation between GluRIIA-RFP and $P_r$ (Pearson r = 0.56, $R^2$ = 0.32, p<0.0001, n = 756 AZs from 8 NMJs from 4 animals, Figure 7B). In contrast, correlation with the levels of GluRIIB-GFP was weaker (Pearson r = 0.32, $R^2$ = 0.1, p<0.0001, n = 756 AZs from 8 NMJs from 4 animals, Figure 7C). A correlation between brighter GluRIIA PSD puncta and higher $P_r$ sites was also observed in the analysis of *syt1* mutants (Figure 3A, arrows). These findings are consistent with previous observations that glutamate receptors preferentially cluster at AZs with

high $P_r$ based on electrophysiological and morphological studies of a *Drosophila* GluRIII hypomorphic mutant (Marrus and Diantonio, 2004). We next examined how the resident AZ protein BRP differentially accumulated at AZs in the dual labeled glutamate receptor subunit lines. After mapping $P_r$ in the larvae, preparations were fixed and stained with anti-BRP antisera. As previously observed in animals lacking tagged glutamate receptors (Figure 1), a positive correlation between AZ $P_r$ and BRP levels was observed (Pearson r = 0.44, $R^2 = 0.2$, $p<0.0001$, n = 399 AZs from 6 NMJs from 4 animals, Figure 7D). In summary, these data indicate that GluRIIA more strongly accumulates at PSDs apposing high $P_r$ AZs.

Beyond the preferential GluRIIA accumulation at high $P_r$ sites, we also observed a change in GluRIIA/GluRIIB distribution within single PSDs. The PSDs apposing the highest $P_r$ AZs showed a skewed distribution of the receptor subtypes, with GluRIIA concentrating in the center of the receptor field immediately apposing the presynaptic BRP cluster (Figure 7E, arrows). At these sites, GluRIIB occupied a more peripheral position around the central GluRIIA cluster. A similar localization pattern with a ring of GluRIIB surrounding a central GluRIIA patch was previously noted with antibody staining for the two receptors at some larval AZs in late 3$^{rd}$ larvae (Marrus et al., 2004). To analyze this segregation in glutamate receptor distribution at single PSDs in greater detail, GluRIIA/B staining was examined in the absence of co-expressed myrGCaMP6s to avoid any overlap in the GFP channel. Our prior analysis (Fig. 7B) indicated the brightest GluRIIA PSDs correspond to high $P_r$ sites. Bright PSDs were selected based on their GluRIIA intensity (2 standard deviations above average) and line profiles were drawn across each PSD defined by their corresponding presynaptic BRP puncta. The intensity of pixels along that line for each fluorophore was then analyzed. Average pixel intensity revealed drastically distinct profiles for GluRIIB distribution between “bright” and

446 "dim" PSDs classified based on their GluRIIA intensity. GluRIIB was more evenly distributed
447 across the entire PSD at dim GluRIIA sites, but was segregated outward, forming a circular
448 donut-like ring around central GluRIIA puncta at bright GluRIIA sites (Figure 7F). In addition,
449 presynaptic BRP intensity was more strongly correlated with postsynaptic GluRIIA levels
450 (Pearson r = 0.53, $R^2$ = 0.28, p<0.0001, n = 2496 AZs from 19 NMJs from 7 animals, Figure 7G)
451 compared to GluRIIB (Pearson r = 0.24, $R^2$ = 0.05, p<0.0001, n = 2496 AZs from 19 NMJs from
452 7 animals, Figure 7H). Overall, these findings indicate the postsynaptic cell accumulates
453 GluRIIA and redistributes GluRIIB to the PSD periphery at high $P_r$ sites.

454

455 **Analysis of *Pr* acquisition during AZ development using glutamate receptor segregation as**
456 **a proxy**

457 The *Drosophila* larval NMJ is a highly dynamic structure, with new synaptic boutons and
458 AZs undergoing continuous addition throughout development (Harris and Littleton, 2015; Rasse
459 et al., 2005; Schuster et al., 1996; Zito et al., 1999). Given the correlation between $Ca^{2+}$ channel
460 density, GluRIIA/GluRIIB segregation and high $P_r$, we were interested in determining how AZs
461 acquire a specific $P_r$ during a larval developmental period that lasts 6-7 days. One model is that
462 certain AZs gain a higher $P_r$ status during development through a tagging or activity-dependent
463 mechanism that would lead to preferential accumulation of key AZ components compared to
464 their neighbors. Alternatively, high $P_r$ AZs might simply be more mature than their low $P_r$
465 neighbors, having an earlier birthdate and a longer timeframe to accumulate AZ material. To
466 differentiate between these models for release heterogeneity, it would be desirable to follow $P_r$
467 development from the embryonic through larval stages. However, this is not technically feasible

468 due to the small size of AZs and the rapid locomotion that larvae undergo, preventing generation
469 of $P_r$ maps in intact moving animals. Instead, we employed an alternative approach to repeatedly
470 image the same NMJ at muscle 26 directly through the cuticle of intact larvae during anesthesia
471 (Andlauer and Sigrist, 2012; Fouquet et al., 2009; Füger et al., 2007; Rasse et al., 2005; Zhang et
472 al., 2010). Using this technique, we found that anesthesia eliminated action potential induced
473 release and the associated GCaMP signals, preventing direct $P_r$ measurements in anesthetized
474 larvae. We instead focused on imaging GluRIIA accumulation and GluRIIA/GluRIIB
475 segregation, which was strongly correlated with $P_r$ (Figure 7), as a proxy for the emergence of
476 high $P_r$ sites. Prior studies demonstrate GluRIIA at PSDs closely tracks with Cac accumulation
477 at corresponding AZs (Fouquet et al., 2009; Rasse et al., 2005), indicating the two compartments
478 are likely to mature at similar rates. To examine this directly, we assayed whether GluRIIA and
479 Cac accumulation were correlated during development. Indeed, the intensity of Cac-GFP and
480 GluRIIA-RFP puncta were strongly correlated at individual AZs during early larval development
481 (Pearson r = 0.823, $R^2$ = 0.6771, p<0.0001, n= 441 AZs from 8 NMJs from 8 larvae, Figure 7 –
482 figure supplement 1A, B), indicating GluRIIA provides a robust marker that reflects the
483 corresponding levels of presynaptic Cac at individual AZs.

484 Previously described *in vivo* imaging approaches with anesthesia at *Drosophila* NMJs
485 employed early 3$^{rd}$ instar larvae as the starting time point, and followed the distribution of
486 fluorescently-labeled synaptic proteins during the final ~36 hours of development prior to
487 pupation (Rasse et al., 2005). To follow AZ $P_r$ development soon after synapse formation, we
488 modified these techniques to allow imaging of glutamate receptor distribution at earlier stages of
489 development (see methods). This allowed successful birth dating and successive imaging of the
490 same AZ over a 6-day period beginning shortly after synapse formation in the early 1$^{st}$ instar

period through the late 3rd instar stage (Figure 8, Figure 8 - figure supplement 1, Figure 8 – figure supplement 2). In early 1st instar larvae (within 12 hours of hatching) GluRIIA and GluRIIB were largely co-localized at postsynaptic puncta (Figure 8, Figure 8 - figure supplement 1). One exception was the presence of diffuse GluRIIA that accumulated around unusually long axonal extensions that emerged from presynaptic boutons (Figure 8A, arrows). These structures were devoid of any detectable GluRIIB or the bright GluRIIA puncta that are associated with AZs, and may be remnants of previously described muscle filopodial structures, termed myopodia, that interact with presynaptic filopodia to dynamically regulate early synaptic target recognition (Kohsaka and Nose, 2009; Ritzenthaler et al., 2000; Ritzenthaler and Chiba, 2003). GluRIIA appears concentrated on these structures, as has been observed for the leucine-rich repeat cell adhesion protein Capricious (Kohsaka and Nose, 2009). Repeated imaging of these thinner GluRIIA-positive processes revealed that they were capable of developing into mature synaptic boutons with concentrated GluRIIA and GluRIIB synaptic puncta (Figure 8 – figure supplement 3). By 24 hours of larval growth, GluRIIA rich extensions were no longer observed, indicating these structures are restricted to early developmental stages.

Live imaging of GluRIIA and GluRIIB distribution at early PSDs in anesthetized 1st instar larvae demonstrated that the receptors were co-localized and lacked the segregation where GluRIIB clustered around central GluRIIA puncta that was observed at high $P_r$ sites later in development (Figure 8B). The first emergence of GluRIIA/B segregation, with GluRIIB rings surrounding a GluRIIA core, was observed after 36 hours of imaging from the 1st instar period (Figure 8B, C). The GluRIIA/B segregation always emerged first at the oldest and most mature synapses that existed previously on the 1st day of imaging (Figure 8B, C). The most mature PSDs also contained more GluRIIA fluorescent signal (17430 ± 634.0, n = 86 AZs from 8 NMJs from

514 5 animals) compared to later born synapses that emerged during the 48 hour imaging session
515 (8909 ± 289.8, n = 210 AZs from 8 NMJs from 5 animals). During later larval development, the
516 cuticle thickness changed dramatically and prevented reliable comparison of absolute receptor
517 density with earlier stages. However it was clear that GluRIIA intensities that were uniform in 1st
518 instar larvae became more heterogeneous at the 3rd instar stage (Figure 8 – figure supplement 2).
519 Indeed, histograms of normalized fluorescence intensity (relative intensity scaled from 0 to 1)
520 revealed that GluRIIA and GluRIIB were distributed relatively uniformly at 1st instar larval
521 PSDs, with GluRIIA distribution becoming more skewed at later stages (Figure 9A, B). These
522 results indicate that GluRIIA/GluRIIB fluorescence distribution is highly heterogeneous by the
523 early 3rd instar stage, with the brightest GluRIIA positive PSDs, and by extension their
524 corresponding high $P_r$ AZs, representing those that appeared earliest in development.

525 Over what time frame do synapses developmentally acquire high $P_r$ properties? To
526 estimate the average time required for this process, the interval from the first emergence of a
527 synapse in an imaging session to the time point when segregation of GluRIIB around GluRIIA
528 central puncta occurred was calculated. This analysis was restricted to newly formed AZs that
529 appeared during the imaging sessions, and excluded AZs that were present in the first imaging
530 session performed in 1st instar larvae. The average time from the first emergence of a synapse to
531 when it acquired the segregated GluRIIA/B pattern observed at high $P_r$ AZs was 3.20 ± 0.08
532 days (n = 41 AZs from 7 NMJs from 3 animals, Figure 9C). In a small subset of PSDs (5%), a
533 slightly faster accumulation of GluRIIA and the formation of GluRIIB peripheral rings was
534 observed, but never faster than 2 days (Figure 8 - figure supplemental 2). Given that the
535 developing NMJ is adding AZs at a rapid rate (Rasse et al., 2005; Schuster et al., 1996), we
536 estimated if AZ maturation time identified over the course of our live imaging experiments

would fit with the 9.9% of high $P_r$ sites observed at the early 3rd instar stage by GCaMP imaging. The number of synapses present at the same NMJ from the 1st instar through the early 3rd instar stage was quantified from live imaging experiments (Figure 9D). AZ number doubled each day, such that the average number of AZs found at the 1st instar stage (day 1) represented 14.7 ± 1.4% (n = 8 NMJs from 3 animals) of all AZs present by day 4 (3 days after initial imaging in 1st instars). This value is similar to the 10% population of high $P_r$ AZs observed during $P_r$ mapping. Overall, these data support the hypothesis that AZ maturation is a key factor in regulating $P_r$, leading to increased accumulation of $Ca^{2+}$ channels and GluRIIA/GluRIIB segregation at high $P_r$ sites compared to AZs that are newly formed (<2 days).

## Discussion

In the current study we used optical quantal imaging to examine the source of heterogeneity in evoked $P_r$ across the AZ population at *Drosophila* NMJs. By combining quantal imaging with SIM microscopy, we first confirmed that release heterogeneity was not caused by summation of fusion events from multiple AZs. By monitoring release over 15 minute intervals, we also observed that $P_r$ was a stable feature of each AZ. The *Drosophila* genome encodes a single member of the N/P/Q-type $Ca^{2+}$ channel α1 subunit family (Cac) that is present at AZs and is responsible for neurotransmitter release (Fouquet et al., 2009; Kawasaki et al., 2004, 2000; Littleton and Ganetzky, 2000; Liu et al., 2011; Rieckhof et al., 2003; Smith et al., 1996). Using transgenically labeled Cac lines, we found that Cac density at AZs strongly correlated with $P_r$. To directly visualize presynaptic $Ca^{2+}$ influx at single AZs, GCaMP fusions to the core AZ component BRP (the *Drosophila* ELKS/CAST homolog) were generated. The levels of $Ca^{2+}$ influx at single AZs was highly correlated with both Cac density and $P_r$. In contrast, loss of the

560 Synaptotagmin 1 synaptic vesicle $Ca^{2+}$ sensor did not change the heterogeneous distribution of $P_r$
561 across AZs.

562 High $P_r$ AZs also displayed a distinct pattern of glutamate receptor clustering. Most PSDs
563 showed a homogeneous distribution of the GluRIIA and GluRIIB containing subunits on the
564 apposing postsynaptic membrane. In contrast, high $P_r$ AZs were apposed by PSDs where
565 GluRIIA receptors concentrated at the center of the AZ, with GluRIIB receptors forming a ring
566 at the PSD periphery. A similar activity-dependent segregation of GluRIIA and a GluRIIA gating
567 mutant has been previously observed at individual AZs in *Drosophila* (Petzoldt et al., 2014). In
568 addition, anti-glutamate receptor antibody staining of wildtype larvae lacking tagged glutamate
569 receptors identified a GluRIIB ring around the GluRIIA core in some mature 3rd instar NMJ AZs
570 (Marrus et al., 2004). The correlation of $P_r$ with GluRIIA accumulation is especially intriguing
571 considering that this subunit has been implicated in homeostatic and activity-dependent plasticity
572 (Davis, 2006; Frank, 2014; Petersen et al., 1997; Sigrist et al., 2003). By following the
573 developmental acquisition of this postsynaptic property as a proxy for $P_r$ from the 1st through 3rd
574 instar larval stages via live imaging, we observed that the earliest formed AZs are the first to
575 acquire this high $P_r$ signature over a time course of ~3 days.

576 Similar to our prior observations (Melom et al., 2013), we found that most AZs at the
577 *Drosophila* NMJ have a low $P_r$. For the current study, the AZ pool was artificially segregated
578 into low and high release sites, with high releasing sites defined based on having a release rate
579 greater than two standard deviations above the mean. Given that birthdate is a key predictor of
580 glutamate receptor segregation, and by proxy $P_r$, we expect the AZ pool to actually reflect a
581 continuum of $P_r$ values based on their developmental history. However, using the two standard
582 deviation criteria, 9.9% of AZs fell into the high $P_r$ category, with an average $P_r$ of 0.28 in

583 extracellular saline containing 1.3 mM $Ca^{2+}$ and 20 mM $MgCl_2$. The remaining AZs that
584 participated in evoked release had an average $P_r$ of 0.05. $Ca^{2+}$ channel density and $Ca^{2+}$ influx at
585 individual AZs was a key determinant of $P_r$ heterogeneity, as evoked $P_r$ and the density of Cac
586 channels tagged with either TdTomato or GFP displayed a strong positive correlation (Pearson r
587 = 0.65 and Pearson r = 0.58, respectively). To bypass any unknown effects of channel tagging on
588 $P_r$, we also created a tool to directly visualize AZ $Ca^{2+}$ influx by tethering GCaMP to the AZ
589 protein BRP. Again, a strong correlation between $Ca^{2+}$ influx and AZ $P_r$ (Pearson r = 0.60) was
590 observed, confirming that the levels of $Ca^{2+}$ influx are a major determinant for synaptic vesicle
591 fusion during an evoked response. Spontaneous fusion showed a much weaker correlation with
592 both Cac density and $Ca^{2+}$ influx at individual AZs, consistent with prior studies indicating
593 spontaneous release rates are poorly correlated with external $Ca^{2+}$ levels at this synapse (Jorquera
594 et al., 2012; Lee et al., 2013). With synaptic vesicle fusion showing a steep non-linear
595 dependence upon external $Ca^{2+}$ with a slope of ~3-4 (Dodge and Rahamimoff, 1967;
596 Heidelberger et al., 1994; Jan and Jan, 1976), a robust change in $P_r$ could occur secondary to a
597 relatively modest increase in $Ca^{2+}$ channel density over development. Although the number of
598 $Ca^{2+}$ channels at a *Drosophila* NMJ AZ is unknown, estimates of Cac-GFP fluorescence during
599 quantal imaging indicate a ~2-fold increase in channel number would be necessary to move a
600 low $P_r$ AZ into the high $P_r$ category. Similar correlations between evoked $P_r$ and $Ca^{2+}$ channel
601 density have been found at mammalian synapses (Holderith et al., 2012; Nakamura et al., 2015;
602 Sheng et al., 2012), suggesting this may represent a common mechanism for determining release
603 strength at synapses.

604 Beyond low and high $P_r$ sites, we found that 9.7% of the AZs analyzed displayed only
605 spontaneous release. We could detect no fusion events for either evoked or spontaneous release

606 for another 14.6% of AZs that were defined by a GluRIIA-positive PSD in live imaging.
607 Whether these cases represent immature AZs with extremely low evoked $P_r$, or distinct
608 categories reflective of differences in AZ content, is unknown. For spontaneous-only sites, we
609 previously found that the $\Delta F/F_{avg}$ quantal signal detected postsynaptically by GCaMP imaging
610 was similar to that observed at mixed mode AZs displaying both evoked and spontaneous events,
611 indicating that there is unlikely to be a dramatic difference in glutamate receptor density at these
612 sites versus low $P_r$ AZs (Melom et al., 2013). Further categorization of spontaneous-only AZs
613 and silent AZs will require the identification of unique makers that can be used to track them in
614 live imaging during synaptic development.

615 Other factors we examined for regulating $P_r$ were differences in local synaptic vesicle
616 pools or synaptic vesicle protein content or state (for example, phosphorylation). $P_r$ was largely
617 unchanged with either 5-minute rest or 5 minute 5 Hz stimulation between imaging sessions.
618 Although $P_r$ may be more dynamic over longer intervals, the observation that developmental
619 maturation of glutamate receptor segregation occurs over ~ 3 days is consistent with $P_r$ being a
620 stable feature of the AZ over shorter time periods (hours to ~1 day). To further examine the role
621 of potential heterogeneity due to differences in synaptic vesicle proteins, we assayed
622 whether $P_r$ heterogeneity was abolished in mutants lacking the $Ca^{2+}$ sensor Synaptotagmin 1, a
623 major regulator of $P_r$ (DiAntonio and Schwarz, 1994; Fernández-Chacón et al., 2001; Geppert et
624 al., 1994; Littleton et al., 1994, 1993; Yoshihara and Littleton, 2002). GCaMP imaging
625 confirmed that release was dramatically reduced and largely asynchronous in *syt1* nulls, and that
626 mini frequency per AZ was increased. Although $P_r$ was reduced in *syt1*, $P_r$ distribution among
627 different AZs remained heterogeneous, suggesting that the AZ, rather than differential
628 distribution of Syt1, is critical. Although roles for other synaptic vesicle proteins in $P_r$

heterogeneity cannot be excluded, the observation that prolonged 5 Hz stimulation, which would be predicted to turn over the synaptic vesicle pool, does not change $P_r$ argues against this hypothesis. Instead, these data support a model that differences in the abundance of presynaptic $Ca^{2+}$ channels underlies heterogeneous AZ $P_r$.

We considered several models for how AZs acquire this heterogeneous nature of $P_r$ distribution. One possibility is that unique AZs gain high $P_r$ status through a mechanism that would result in preferential accumulation of key AZ components compared to their neighbors. Given that retrograde signaling from the muscle is known to drive synaptic development at *Drosophila* NMJs (Ball et al., 2010; Berke et al., 2013; Harris and Littleton, 2015; Keshishian and Kim, 2004; McCabe et al., 2003; Piccioli and Littleton, 2014; Yoshihara et al., 2005), certain AZ populations might have preferential access to specific signaling factors that would alter their $P_r$ state. Another model is that AZs compete for key presynaptic $P_r$ regulators through an activity-dependent process. Once an AZ achieves a slight imbalance over its neighbors in release strength, it would then "win" and preferentially accumulate AZ material, similar to the concept of synapse elimination during motor neuron competition at mammalian NMJs (Tapia et al., 2012). Finally, high $P_r$ AZs might simply be more mature than their low $P_r$ neighbors, having a longer timeframe to accumulate AZ components. This model would not require any AZ to gain a favored status. AZs that appeared first during development would have more time to accumulate AZ material at a rate that would be largely identical over all AZs. Given that the *Drosophila* NMJ is constantly forming new AZs at a rapid pace during development (Rasse et al., 2005; Schuster et al., 1996), newly formed AZs would take longer to mature, generating a population of "older" AZs that would increase their $P_r$ at the same proportional rate as their newer neighbors. Given that GCaMP imaging indicates high $P_r$ sites segregate GluRIIA and GluRIIB

differently from low $P_r$ sites, with the IIA isoform preferentially localizing at the center of PSDs apposing high $P_r$ AZs, we used developmental acquisition of this property as an indicator of high $P_r$ sites. Although segregation of glutamate receptors may not perfectly replicate the timing of $P_r$ acquisition during development, it is currently the best tool we have at our disposal for sequential live imaging. Based on the acquisition of GluRIIA/GluRIIB segregation, our data support the model that increases in $P_r$ reflect a time-dependent maturation process at the NMJ. Indeed, AZs that developed later in imaging sessions showed a similar time course for acquiring the postsynaptic segregation of glutamate receptors, indicating a fixed developmental maturation from low to high $P_r$ AZs that is likely to account for the majority of release heterogeneity at this connection. The continuous addition of new AZs, which double during each day of development, ensures that the overall ratio of high to low $P_r$ sites remain relatively fixed at a low percentage, depending on developmental stage and the rate of new AZ addition.

We did not test the correlation of $P_r$ with other AZ proteins besides Cac and BRP, but it would not be surprising to see a positive correlation with the density of many AZ proteins based on the observation that maturation time is a key determinant for $P_r$. AZ maturation is also likely to promote increased synaptic vesicle docking and availability, consistent with observations that correlate active zone size with either $P_r$ or the readily releasable pool (Han et al., 2011; Holderith et al., 2012; Matkovic et al., 2013; Matz et al., 2010; Nakamura et al., 2015; Schikorski and Stevens, 1997; Wadel et al., 2007). Although it is poorly understood how AZs are assembled during development, our data would not support a model that AZs are fully preassembled during transport and then deposited as a single “quantal” entity onto the presynaptic membrane. Rather, these data support a model of seeding of AZ material that increases developmentally over time as AZs matures, consistent with several studies of AZ development in *Drosophila* (Böhme et al.,

675 2016; Fouquet et al., 2009). In theory, each AZ would have equal access to new AZ material, and
676 accumulate it at a fairly constant rate, with birthdate being the primary factor in how much AZ
677 material they contain, and correspondingly, their $P_r$ status. Although no evidence for rapid
678 changes in $P_r$ were detected in the steady-state conditions used in the current study, homeostatic
679 plasticity is known to alter $P_r$ over a rapid time frame (~10 minutes) at the NMJ (Davis and
680 Müller, 2015; Frank, 2014; Frank et al., 2006). It will be interesting to determine if Cac density
681 can change over such a rapid window, or whether the enhanced release is mediated solely
682 through changes in Cac function and $Ca^{2+}$ influx (Müller and Davis, 2012). Changes in the
683 temporal order of $P_r$ development could also occur secondary to altered transport or capture of
684 AZ material. For example, the large NMJ on muscle fibers 6 and 7 displays a gradient in
685 synaptic transmission, with terminal branch boutons often showing a larger population of higher
686 $P_r$ AZs (Guerrero et al., 2005; Peled and Isacoff, 2011). If AZ material is not captured by earlier
687 synapses along the arbor, it would be predicted to accumulate in terminal boutons, potentially
688 allowing these AZs greater access to key components, and subsequently increasing their rate of
689 $P_r$ acquisition. In summary, our data indicate that $Ca^{2+}$ channel density and $Ca^{2+}$ influx at single
690 AZs is a key determinant for release heterogeneity, and that developmental AZ maturation is a
691 key factor in $P_r$ at the *Drosophila* NMJ.
692

693 **Materials and methods**

694 *Drosophila stocks*

695 Flies were cultured at 25°C on standard medium. Actively crawling 3rd instar male and female
696 larvae dwelling on top of the food were used for experiments unless noted. The following strains
697 were used: UAS-myrGCaMP6s, UAS- GCaMP6m-BRPshort, pBid-lexAop-myrGcaMP6s, UAS-
698 myrjRGECO; Elav–GAL4, Mef2–GAL4, UAS-CacGFP (provided by Richard Ordway); UAS-
699 CacTdTomato (provided by Richard Ordway); GluRIIA-RFP (provided by Stephan Sigrist),
700 GluRIIB-GFP (provided by Stephan Sigrist) and 44H10-LexAp65 (provided by Gerald Rubin).
701 *syt1* null mutants were generated by crossing $syt1^{N13}$, an intragenic *syt1* deficiency (Littleton et
702 al., 1994), with $syt1^{AD4}$, which truncates Syt1 before the transmembrane domain (DiAntonio and
703 Schwarz, 1994).

704

705 *Transgenic constructs*

706 The fluorescent $Ca^{2+}$ sensor GCaMP6s was tethered to the plasma membrane with an N-terminal
707 myristoylation (myr) sequence. The first 90 amino acids of Src64b, containing a myristoylation
708 target sequence, were subcloned into pBID-UASc with EcoRI and BglII (creating pBID-UASc-
709 myr). GCaMP6s cDNA (Addgene plasmid 40753) was cloned into pBID-UASc-myr with BglII
710 and XbaI. To generate the UAS-GCaMP6m-Brp-short line, GCaMP6m (Addgene plasmid
711 40754) cDNA and Brp-short (gift from Dr. Tobias Rasse) were PCR amplified and double
712 digested with EcoRI/BglII and BglII/XbaI, respectively. The two cDNA fragments were ligated
713 and the product was used to PCR amplify the fused GCaMP6m-Brp-short cDNA. The PCR

product was inserted into the vector backbone pBID-UASc after digestion with EcoRI and XbaI to generate the final plasmid pBID-UASc-GCaMP6m-Brp-short. To create UAS-myrjRGECO, the vector backbone pBID-UASc-myr was digested with BglII and XbaI. jRGECO sequence was amplified from plasmid pGP-CMV-NES-jRGECO1a (gift from Dr. Douglas Kim, Addgene plasmid #61563). The digested backbone and insert were fused according to the Gibson assembly protocol using NEBuilder HighFidelity DNA Assembly Cloning Kit (E5520). To generate pBid-lexAop-myrGcaMP6s, myrGCaMP6s was amplified by PCR and inserted into pBiD-lexAop-DSCP (gift from Brian McCabe) between NotI and XbaI sites. All transgenic *Drosophila* strains were generated by BestGene.

*Immunocytochemistry*

Wandering 3$^{rd}$ instar larvae were dissected in $Ca^{2+}$-free HL3 solution and fixed in 4% paraformaldehyde for 10 minutes, washed in PBT (PBS plus 0.1% Triton X-100) and blocked in 5% normal goat serum (NGS) and 5% BSA in PBT for 15 minutes. Samples were incubated overnight with anti-BRP (NC82, 1:200) from the Developmental Studies Hybridoma Bank, washed for 1 hour in PBS and then incubated for 2-3 hours with Alexa Fluor 607-conjugated anti-mouse IgG at 1:1000 (Invitrogen).

*Confocal imaging and data analysis*

Confocal images were obtained on a Zeiss Axio Imager 2 equipped with a spinning-disk confocal head (CSU-X1; Yokagawa) and ImagEM X2 EM-CCD camera (Hammamatsu). An

735 Olympus LUMFL N 60X objective with a 1.10 NA was used to acquire GCaMP6s imaging data
736 at 7 to 8 Hz. A Zeiss pan-APOCHROMAT 63X objective with 1.40 NA was used for imaging
737 stained or live animals. 3$^{rd}$ instar larvae were dissected in $Ca^{2+}$-free HL3 containing 20 mM
738 $MgCl_2$. After dissection, preparations were maintained in HL3 with 20 mM $MgCl_2$ and 1.3 mM
739 $Ca^{2+}$ for 5 minutes. To stimulate the NMJ, motor nerves were cut close to the ventral ganglion
740 and sucked into a pipette. Single pulses of current were delivered every one second for myr-
741 jRGECO mapping or every three seconds for GCaMP6s mapping with an AMPI Master-8
742 stimulator using a stimulus strength just above the threshold for evoking EJPs. A 3D image stack
743 was taken before the GCaMP imaging session to generate a full map of GluRIIA or Cac channel
744 distribution. Later, single focal planes were imaged continuously for 4 –5 minutes to collect
745 GCaMP signals. Volocity 3D Image Analysis software (PerkinElmer) was used to analyze
746 images. All images were Gaussian filtered (fine) to reduce noise and a movement-correction
747 algorithm was applied. To enhance identification of myrGCaMP6 flashes, background
748 myrGCaMP fluorescence was subtracted by creating a composite stack of 5–6 images during
749 intervals when no synaptic release occurred. To identify the position of GluRIIA receptors and
750 corresponding $Ca^{2+}$ events, a 3D stack image of GluRIIA was merged to create a single plane.
751 AZ position was identified using the "find spot" algorithm in Volocity 3.2 software that detects
752 fluorescent peaks. ROIs with identical 5-pixel size (0.138 µm/pixel) were automatically
753 generated by the software from identified GluRIIA spots. All GCaMP flashes were detected
754 using the intensity threshold tool and assigned to specific ROIs based on proximity of their
755 centroids. The time and location of $Ca^{2+}$ events were imported into Excel or Matlab for further
756 analysis. The number of observed GCaMP events per AZ was divided by the number of
757 delivered stimuli to calculate AZ $P_r$. Analysis of Cac, BRP, GluRIIA or GluRIIB intensities was

758 performed similarly, identifying AZ fluorescence peaks and defining 3 pixel square ROIs around
759 each peak to calculate average fluorescence. Average AZ fluorescence intensities of 3-pixel
760 square ROIs was also used for correlation analysis.

761

762 *Live imaging*

763 Larvae were anesthetized with SUPRANE (desflurane, USP) from Amerinet Choice (Zhang et
764 al., 2010). Larvae were incubated in a petri dish with a small paper towel containing Suprane for
765 1-2 minutes in a fume hood. Anesthetized larvae were positioned ventral side up on a glass slide
766 between spacers made by transparent tape, which prevented extreme compression of the larvae.
767 Different size spacers were required for the various larval stages. Larvae were covered with a
768 thin film of halocarbon oil and then with a cover glass. NMJ synapses on muscle 26 in hemi-
769 segment 2 or 3 were imaged. After an imaging session, larvae were placed in numbered
770 chambers with food in a 25°C incubator. The same data acquisition settings where used to
771 visualize NMJs at different larval stages. Larvae were imaged with either 6, 24 and 36 hours
772 intervals for one data set (Figure 8 A-C), or for 24 hours intervals for the remaining datasets. To
773 keep the size consistent between different time periods, images of the corresponding NMJ area at
774 younger stages were cut (dashed areas in figures) and placed onto a black background. This
775 presentation generated a similar orientation of the different size NMJs for easier comparison for
776 Figure 8, Figure 9 and Figure 8-supplemental figure 2.

777

778 *Statistical analysis*

779 Statistical analysis was performed with GraphPad Prism using one-way ANOVA for comparison
780 of samples within an experimental group, or Student's t-test for comparing two groups. Asterisks
781 denote p-values of: *, P≤0.05; **, P≤0.01; and ***, P≤0.001. All histograms and measurements
782 are shown as mean ± SEM. Pearson coefficient of correlation was calculated in GraphPad Prism
783 using the following parameters: - two-tailed P value and 95% confidence interval.

784

785 **Acknowledgements**

786 This work was supported by NIH grant MH104536 to J.T.L. K.L.C. was supported in part by
787 NIH pre-doctoral training grant T32GM007287. We thank the Bloomington *Drosophila* Stock
788 Center (NIH P40OD018537), the Developmental Studies Hybridoma Bank, Richard Ordway
789 (Penn State University) and Stephan Sigrist (Freie Univesitat Berlin) for providing *Drosophila*
790 strains, Eliza Vasile (Koch Institute) for help with SIM data acquisition, and members of the
791 Littleton lab for helpful discussions and comments on the manuscript.

792

793

## References

Acuna, C., Liu, X., Südhof, T.C., 2016. How to Make an Active Zone: Unexpected Universal Functional Redundancy between RIMs and RIM-BPs. Neuron 91, 792–807. doi:10.1016/j.neuron.2016.07.042

Andlauer, T.F.M. and Sigrist, S.J. 2012. *In vivo* imaging of *Drosophila* larval neuromuscular junctions to study synapse assembly. Cold Spring Harb Protoc 2012, 407–413. doi:10.1101/pdb.top068577

Atwood, H.L., Karunanithi, S., 2002. Diversification of synaptic strength: presynaptic elements. Nat Rev Neurosci 3, 497–516. doi:10.1038/nrn876

Augustine, G.J., Charlton, M.P., Smith, S.J., 1985. Calcium entry and transmitter release at voltage-clamped nerve terminals of squid. J Physiol (Lond) 367, 163–181.

Ball, R.W., Warren-Paquin, M., Tsurudome, K., Liao, E.H., Elazzouzi, F., Cavanagh, C., An, B.-S., Wang, T.-T., White, J.H., Haghighi, A.P., 2010. Retrograde BMP signaling controls synaptic growth at the NMJ by regulating trio expression in motor neurons. Neuron 66, 536–549. doi:10.1016/j.neuron.2010.04.011

Berke, B., Wittnam, J., McNeill, E., Van Vactor, D.L., Keshishian, H., 2013. Retrograde BMP signaling at the synapse: a permissive signal for synapse maturation and activity-dependent plasticity. J Neurosci 33, 17937–17950. doi:10.1523/JNEUROSCI.6075-11.2013

Böhme, M.A., Beis, C., Reddy-Alla, S., Reynolds, E., Mampell, M.M., Grasskamp, A.T., Lützkendorf, J., Bergeron, D.D., Driller, J.H., Babikir, H., Göttfert, F., Robinson, I.M., O'Kane, C.J., Hell, S.W., Wahl, M.C., Stelzl, U., Loll, B., Walter, A.M., Sigrist, S.J., 2016. Active zone scaffolds differentially accumulate Unc13 isoforms to tune Ca(2+) channel-vesicle coupling. Nat Neurosci 19, 1311–1320. doi:10.1038/nn.4364

Branco, T., Staras, K., 2009. The probability of neurotransmitter release: variability and feedback control at single synapses. Nat Rev Neurosci 10, 373–383. doi:10.1038/nrn2634

Bruckner, J.J., Gratz, S.J., Slind, J.K., Geske, R.R., Cummings, A.M., Galindo, S.E., Donohue, L.K., O'Connor-Giles, K.M., 2012. Fife, a *Drosophila* Piccolo-RIM homolog, promotes active zone organization and neurotransmitter release. J Neurosci 32, 17048–17058. doi:10.1523/JNEUROSCI.3267-12.2012

Bruckner, J.J., Zhan, H., Gratz, S.J., Rao, M., Ukken, F., Zilberg, G., O'Connor-Giles, K.M., 2017. Fife organizes synaptic vesicles and calcium channels for high-probability neurotransmitter release. J Cell Biol 216, 231–246. doi:10.1083/jcb.201601098

Bucurenciu, I., Kulik, A., Schwaller, B., Frotscher, M., Jonas, P., 2008. Nanodomain coupling

between Ca2+ channels and Ca2+ sensors promotes fast and efficient transmitter release at a cortical GABAergic synapse. Neuron 57, 536–545. doi: 10.1016/ j.neuron.2007.12.026

Catterall, W.A., Few, A.P., 2008. Calcium channel regulation and presynaptic plasticity. Neuron 59, 882–901. doi:10.1016/j.neuron.2008.09.005

Chen, K., Featherstone, D.E., 2005. Discs-large (DLG) is clustered by presynaptic innervation and regulates postsynaptic glutamate receptor subunit composition in *Drosophila*. BMC Biol 3, 1. doi:10.1186/1741-7007-3-1

Chen, Z., Das, B., Nakamura, Y., DiGregorio, D.A., Young, S.M., 2015. $Ca^{2+}$ channel to synaptic vesicle distance accounts for the readily releasable pool kinetics at a functionally mature auditory synapse. J Neurosci 35, 2083–2100. doi:10.1523/JNEUROSCI.2753-14.2015

Cho, R.W., Buhl, L.K., Volfson, D., Tran, A., Li, F., Akbergenova, Y., Littleton, J.T., 2015. Phosphorylation of Complexin by PKA Regulates Activity-Dependent Spontaneous Neurotransmitter Release and Structural Synaptic Plasticity. Neuron 88, 749–761. doi:10.1016/j.neuron.2015.10.011

Dana, H., Mohar, B., Sun, Y., Narayan, S., Gordus, A., Hasseman, J.P., Tsegaye, G., Holt, G.T., Hu, A., Walpita, D., Patel, R., Macklin, J.J., Bargmann, C.I., Ahrens, M.B., Schreiter, E.R., Jayaraman, V., Looger, L.L., Svoboda, K., Kim, D.S., 2016. Sensitive red protein calcium indicators for imaging neural activity. elife 5. doi:10.7554/eLife.12727

Davis, G.W., 2006. Homeostatic control of neural activity: from phenomenology to molecular design. Annu Rev Neurosci 29, 307–323. doi:10.1146/annurev.neuro.28.061604.135751

Davis, G.W., Müller, M., 2015. Homeostatic control of presynaptic neurotransmitter release. Annu Rev Physiol 77, 251–270. doi:10.1146/annurev-physiol-021014-071740

DiAntonio, A., Petersen, S.A., Heckmann, M., Goodman, C.S., 1999. Glutamate receptor expression regulates quantal size and quantal content at the *Drosophila* neuromuscular junction. J. Neurosci. 19, 3023--3032.

DiAntonio, A., Schwarz, T.L., 1994. The effect on synaptic physiology of synaptotagmin mutations in *Drosophila*. Neuron 12, 909–920.

Dodge, F.A., Rahamimoff, R., 1967. Co-operative action a calcium ions in transmitter release at the neuromuscular junction. J Physiol (Lond) 193, 419–432.

Dolphin, A.C., Huston, E., Pearson, H., Menon-Johanssen, A., Sweeney, M.I., Adams, M.E., Scott, R.H., 1991. G protein modulation of calcium entry and transmitter release. Ann N Y Acad Sci 635, 139–152.

862 Eggermann, E., Bucurenciu, I., Goswami, S.P., Jonas, P., 2011. Nanodomain coupling between
863 $Ca^{2+}$ channels and sensors of exocytosis at fast mammalian synapses. Nat Rev Neurosci
864 13, 7–21. doi:10.1038/nrn3125

865 Ehmann, N., van de Linde, S., Alon, A., Ljaschenko, D., Keung, X.Z., Holm, T., Rings, A.,
866 DiAntonio, A., Hallermann, S., Ashery, U., Heckmann, M., Sauer, M., Kittel, R.J., 2014.
867 Quantitative super-resolution imaging of Bruchpilot distinguishes active zone states. Nat
868 Commun 5, 4650. doi:10.1038/ncomms5650

869 Éltes, T., Kirizs, T., Nusser, Z., Holderith, N., 2017. Target Cell Type-Dependent Differences in
870 Ca(2+) Channel Function Underlie Distinct Release Probabilities at Hippocampal
871 Glutamatergic Terminals. J Neurosci 37, 1910–1924. doi:10.1523/JNEUROSCI.2024-
872 16.2017

873 Evans, R.M., Zamponi, G.W., 2006. Presynaptic $Ca^{2+}$ channels--integration centers for neuronal
874 signaling pathways. Trends Neurosci 29, 617–624. doi:10.1016/j.tins.2006.08.006

875 Featherstone, D.E., Rushton, E., Rohrbough, J., Liebl, F., Karr, J., Sheng, Q., Rodesch, C.K.,
876 Broadie, K., 2005. An essential *Drosophila* glutamate receptor subunit that functions in
877 both central neuropil and neuromuscular junction. J. Neurosci. 25, 3199--3208.

878 Feeney, C.J., Karunanithi, S., Pearce, J., Govind, C.K., Atwood, H.L., 1998. Motor nerve
879 terminals on abdominal muscles in larval flesh flies, Sarcophaga bullata: comparisons
880 with *Drosophila*. J Comp Neurol 402, 197–209. doi:10.1002/(SICI)1096-
881 9861(19981214)402:2<197::AID-CNE5>3.0.CO;2-Q

882 Fernández-Chacón, R., Königstorfer, A., Gerber, S.H., García, J., Matos, M.F., Stevens, C.F.,
883 Brose, N., Rizo, J., Rosenmund, C., Südhof, T.C., 2001. Synaptotagmin I functions as a
884 calcium regulator of release probability. Nature 410, 41–49. doi:10.1038/35065004

885 Fouquet, W., Owald, D., Wichmann, C., Mertel, S., Depner, H., Dyba, M., Hallermann, S.,
886 Kittel, R.J., Eimer, S., Sigrist, S.J., 2009. Maturation of active zone assembly by
887 Drosophila Bruchpilot. J Cell Biol 186, 129–145. doi:10.1083/jcb.200812150

888 Frank, C.A., 2014. Homeostatic plasticity at the *Drosophila* neuromuscular junction.
889 Neuropharmacology 78, 63–74. doi:10.1016/j.neuropharm.2013.06.015

890 Frank, C.A., Kennedy, M.J., Goold, C.P., Marek, K.W., Davis, G.W., 2006. Mechanisms
891 underlying the rapid induction and sustained expression of synaptic homeostasis. Neuron
892 52, 663–677. doi:10.1016/j.neuron.2006.09.029

893 Füger, P., Behrends, L.B., Mertel, S., Sigrist, S.J. and Rasse, T.M., 2007. Live imaging of
894 synapse development and measuring protein dynamics using two-color fluorescence
895 recovery after photo-bleaching at *Drosophila* synapses. Nat Protoc 2, 3285–3298.

doi:10.1038/nprot.2007.472

Geppert, M., Goda, Y., Hammer, R.E., Li, C., Rosahl, T.W., Stevens, C.F., Südhof, T.C., 1994. Synaptotagmin I: a major $Ca^{2+}$ sensor for transmitter release at a central synapse. Cell 79, 717–727. doi:10.1016/0092-8674(94)90556-8

Glebov, O.O., Jackson, R.E., Winterflood, C.M., Owen, D.M., Barker, E.A., Doherty, P., Ewers, H. and Burrone, J., 2017. Nanoscale structural plasticity of the active zone matrix modulates presynaptic function. Cell Rep 18, 2715–2728. doi:10.1016/j.celrep.2017.02.064

Graf, E.R., Valakh, V., Wright, C.M., Wu, C., Liu, Z., Zhang, Y.Q., DiAntonio, A., 2012. RIM promotes calcium channel accumulation at active zones of the *Drosophila* neuromuscular junction. J Neurosci 32, 16586–16596. doi:10.1523/JNEUROSCI.0965-12.2012

Graf, E.R., Valakh, V., Wright, C.M., Wu, C., Liu, Z., Zhang, Y.Q. and DiAntonio, A., 2009. Rab3 dynamically controls protein composition at active zones. Neuron 64, 663–677. doi:10.1016/j.neuron.2009.11.002

Guan, Z., Bykhovskaia, M., Jorquera, R.A., Sutton, R.B., Akbergenova, Y., Littleton, J.T., 2017. A synaptotagmin suppressor screen indicates SNARE binding controls the timing and $Ca^{2+}$ cooperativity of vesicle fusion. elife 6. doi:10.7554/eLife.28409

Guerrero, G., Reiff, D.F., Agarwal, G., Ball, R.W., Borst, A., Goodman, C.S., Isacoff, E.Y., 2005. Heterogeneity in synaptic transmission along a *Drosophila* larval motor axon. Nat Neurosci 8, 1188–1196. doi:10.1038/nn1526

Han, Y., Kaeser, P.S., Südhof, T.C., Schneggenburger, R., 2011. RIM determines $Ca^{2+}$ channel density and vesicle docking at the presynaptic active zone. Neuron 69, 304–316. doi:10.1016/j.neuron.2010.12.014

Harris, K.P., Littleton, J.T., 2015. Transmission, development, and plasticity of synapses. Genetics 201, 345–375. doi:10.1534/genetics.115.176529

Heidelberger, R., Heinemann, C., Neher, E., Matthews, G., 1994. Calcium dependence of the rate of exocytosis in a synaptic terminal. Nature 371, 513–515. doi:10.1038/371513a0

Holderith, N., Lorincz, A., Katona, G., Rózsa, B., Kulik, A., Watanabe, M., Nusser, Z., 2012. Release probability of hippocampal glutamatergic terminals scales with the size of the active zone. Nat Neurosci 15, 988–997. doi:10.1038/nn.3137

Jan, L.Y., Jan, Y.N., 1976. Properties of the larval neuromuscular junction in *Drosophila* melanogaster. J Physiol (Lond) 262, 189–214.

Johansen, J., Halpern, M.E., Johansen, K.M., Keshishian, H., 1989. Stereotypic morphology of

glutamatergic synapses on identified muscle cells of *Drosophila* larvae. J Neurosci 9, 710–725.

Jorquera, R.A., Huntwork-Rodriguez, S., Akbergenova, Y., Cho, R.W., Littleton, J.T., 2012. Complexin controls spontaneous and evoked neurotransmitter release by regulating the timing and properties of synaptotagmin activity. J Neurosci 32, 18234–18245. doi:10.1523/JNEUROSCI.3212-12.2012

Katz, B., Miledi, R., 1967. The timing of calcium action during neuromuscular transmission. J Physiol (Lond) 189, 535–544. doi:10.1113/jphysiol.1967.sp008183

Katz, B., Miledi, R., 1969. Spontaneous and evoked activity of motor nerve endings in calcium Ringer. J Physiol (Lond) 203, 689–706.

Katz, B.S., 1969. The Release of Neural Transmitter Substances (Sherrington Lecture): Bernard S. Katz: 9780853230601: Amazon.com: Books. Liverpool University Press.

Kaufmann, N., DeProto, J., Ranjan, R., Wan, H., Van Vactor, D., 2002. *Drosophila* liprin-alpha and the receptor phosphatase Dlar control synapse morphogenesis. Neuron 34, 27–38. doi:10.1016/S0896-6273(02)00643-8

Kawasaki, F., Felling, R., Ordway, R.W., 2000. A temperature-sensitive paralytic mutant defines a primary synaptic calcium channel in *Drosophila*. J Neurosci 20, 4885–4889.

Kawasaki, F., Zou, B., Xu, X., Ordway, R.W., 2004. Active zone localization of presynaptic calcium channels encoded by the *cacophony* locus of *Drosophila*. J Neurosci 24, 282–285. doi:10.1523/JNEUROSCI.3553-03.2004

Keller, D., Babai, N., Kochubey, O., Han, Y., Markram, H., Schürmann, F., Schneggenburger, R., 2015. An Exclusion Zone for $Ca^{2+}$ Channels around Docked Vesicles Explains Release Control by Multiple Channels at a CNS Synapse. PLoS Comput Biol 11, e1004253. doi:10.1371/journal.pcbi.1004253

Keshishian, H., Kim, Y.-S., 2004. Orchestrating development and function: retrograde BMP signaling in the *Drosophila* nervous system. Trends Neurosci 27, 143–147. doi:10.1016/j.tins.2004.01.004

Kittel, R.J., Wichmann, C., Rasse, T.M., Fouquet, W., Schmidt, M., Schmid, A., Wagh, D.A., Pawlu, C., Kellner, R.R., Willig, K.I., Hell, S.W., Buchner, E., Heckmann, M., Sigrist, S.J., 2006. Bruchpilot promotes active zone assembly, $Ca^{2+}$ channel clustering, and vesicle release. Science 312, 1051–1054. doi:10.1126/science.1126308

Kohsaka, H., Nose, A., 2009. Target recognition at the tips of postsynaptic filopodia: accumulation and function of Capricious. Development (Cambridge, England) 136, 1127--1135.

963 Körber, C., Kuner, T., 2016. Molecular machines regulating the release probability of synaptic
964 vesicles at the active zone. Front Synaptic Neurosci 8, 5. doi:10.3389/fnsyn.2016.00005

965 Lee, J., Guan, Z., Akbergenova, Y., Littleton, J.T., 2013. Genetic analysis of synaptotagmin C2
966 domain specificity in regulating spontaneous and evoked neurotransmitter release. J
967 Neurosci 33, 187–200. doi:10.1523/JNEUROSCI.3214-12.2013

968 Littleton, J.T., Ganetzky, B., 2000. Ion channels and synaptic organization: analysis of the
969 Drosophila genome. Neuron 26, 35–43.

970 Littleton, J.T., Stern, M., Perin, M., Bellen, H.J., 1994. Calcium dependence of neurotransmitter
971 release and rate of spontaneous vesicle fusions are altered in *Drosophila* synaptotagmin
972 mutants. Proc Natl Acad Sci U S A 91, 10888–10892.

973 Littleton, J.T., Stern, M., Schulze, K., Perin, M., Bellen, H.J., 1993. Mutational analysis of
974 *Drosophila* synaptotagmin demonstrates its essential role in $Ca^{2+}$-activated
975 neurotransmitter release. Cell 74, 1125–1134.

976 Liu, K.S.Y., Siebert, M., Mertel, S., Knoche, E., Wegener, S., Wichmann, C., Matkovic, T.,
977 Muhammad, K., Depner, H., Mettke, C., Bückers, J., Hell, S.W., Müller, M., Davis,
978 G.W., Schmitz, D., Sigrist, S.J., 2011. RIM-binding protein, a central part of the active
979 zone, is essential for neurotransmitter release. Science 334, 1565–1569.
980 doi:10.1126/science.1212991

981 Liu, S., Liu, Q., Tabuchi, M., Wu, M.N., 2016. Sleep drive is encoded by neural plastic changes
982 in a dedicated circuit. Cell 165, 1347–1360. doi:10.1016/j.cell.2016.04.013

983 Marrus, S.B., Diantonio, A., 2004. Preferential localization of glutamate receptors opposite sites
984 of high presynaptic release. Curr. Biol. 14, 924--931.

985 Marrus, S.B., Portman, S.L., Allen, M.J., Moffat, K.G., Diantonio, A., 2004. Differential
986 localization of glutamate receptor subunits at the *Drosophila* neuromuscular junction. J.
987 Neurosci. 24, 1406--1415.

988 Marrus, S.C.O.T.T.B., DiAntonio, A.A.R.O.N., 2004. Preferential localization of glutamate
989 receptors opposite sites of high presynaptic release. Curr Biol 14, 924–931.
990 doi:10.1016/j.cub.2004.05.047

991 Maschi, D., Klyachko, V.A., 2017. Spatiotemporal regulation of synaptic vesicle fusion sites in
992 central synapses. Neuron 94, 65–73.e3. doi:10.1016/j.neuron.2017.03.006

993 Matkovic, T., Siebert, M., Knoche, E., Depner, H., Mertel, S., Owald, D., Schmidt, M., Thomas,
994 U., Sickmann, A., Kamin, D., Hell, S.W., Bürger, J., Hollmann, C., Mielke, T.,
995 Wichmann, C., Sigrist, S.J., 2013. The Bruchpilot cytomatrix determines the size of the
996 readily releasable pool of synaptic vesicles. J Cell Biol 202, 667–683.

997 doi:10.1083/jcb.201301072

998 Matz, J., Gilyan, A., Kolar, A., McCarvill, T., Krueger, S.R., 2010. Rapid structural alterations
999 of the active zone lead to sustained changes in neurotransmitter release. Proc Natl Acad
1000 Sci U S A 107, 8836–8841. doi:10.1073/pnas.0906087107

1001 McCabe, B.D., Marqués, G., Haghighi, A.P., Fetter, R.D., Crotty, M.L., Haerry, T.E., Goodman,
1002 C.S., O'Connor, M.B., 2003. The BMP homolog Gbb provides a retrograde signal that
1003 regulates synaptic growth at the *Drosophila* neuromuscular junction. Neuron 39, 241–
1004 254. doi:10.1016/S0896-6273(03)00426-4

1005 Meinrenken, C.J., Borst, J.G.G., Sakmann, B., 2002. Calcium secretion coupling at calyx of Held
1006 governed by nonuniform channel-vesicle topography. J Neurosci 22, 1648–1667.

1007 Meinrenken, C.J., Borst, J.G.G., Sakmann, B., 2003. Local routes revisited: the space and time
1008 dependence of the $Ca^{2+}$ signal for phasic transmitter release at the rat calyx of Held. J
1009 Physiol (Lond) 547, 665–689. doi:10.1113/jphysiol.2002.032714

1010 Melom, J.E., Akbergenova, Y., Gavornik, J.P., Littleton, J.T., 2013. Spontaneous and evoked
1011 release are independently regulated at individual active zones. J Neurosci 33, 17253–
1012 17263. doi:10.1523/JNEUROSCI.3334-13.2013

1013 Muhammad, K., Reddy-Alla, S., Driller, J.H., Schreiner, D., Rey, U., Böhme, M.A., Hollmann,
1014 C., Ramesh, N., Depner, H., Lützkendorf, J., Matkovic, T., Götz, T., Bergeron, D.D.,
1015 Schmoranzer, J., Goettfert, F., Holt, M., Wahl, M.C., Hell, S.W., Scheiffele, P., Walter,
1016 A.M., Loll, B., Sigrist, S.J., 2015. Presynaptic spinophilin tunes neurexin signalling to
1017 control active zone architecture and function. Nat Commun 6, 8362.
1018 doi:10.1038/ncomms9362

1019 Müller, M., Davis, G.W., 2012. Transsynaptic control of presynaptic $Ca^{2+}$ influx achieves
1020 homeostatic potentiation of neurotransmitter release. Curr Biol 22, 1102–1108.
1021 doi:10.1016/j.cub.2012.04.018

1022 Nakamura, Y., Harada, H., Kamasawa, N., Matsui, K., Rothman, J.S., Shigemoto, R., Silver,
1023 R.A., DiGregorio, D.A., Takahashi, T., 2015. Nanoscale distribution of presynaptic
1024 Ca(2+) channels and its impact on vesicular release during development. Neuron 85,
1025 145–158. doi:10.1016/j.neuron.2014.11.019

1026 Newman, Z.L., Hoagland, A., Aghi, K., Worden, K., Levy, S.L., Son, J.H., Lee, L.P., Isacoff,
1027 E.Y., 2017. Input-Specific Plasticity and Homeostasis at the *Drosophila* Larval
1028 Neuromuscular Junction. Neuron 93, 1388–1404.e10. doi:10.1016/j.neuron.2017.02.028

1029 Owald, D., Fouquet, W., Schmidt, M., Wichmann, C., Mertel, S., Depner, H., Christiansen, F.,
1030 Zube, C., Quentin, C., Körner, J., Urlaub, H., Mechtler, K., Sigrist, S.J., 2010. A Syd-1

homologue regulates pre- and postsynaptic maturation in *Drosophila*. J Cell Biol 188, 565–579. doi:10.1083/jcb.200908055

Owald, D., Khorramshahi, O., Gupta, V.K., Banovic, D., Depner, H., Fouquet, W., Wichmann, C., Mertel, S., Eimer, S., Reynolds, E., Holt, M., Aberle, H., Sigrist, S.J., 2012. Cooperation of Syd-1 with Neurexin synchronizes pre- with postsynaptic assembly. Nat Neurosci 15, 1219–1226. doi:10.1038/nn.3183

Peled, E.S., Isacoff, E.Y., 2011. Optical quantal analysis of synaptic transmission in wild-type and rab3-mutant *Drosophila* motor axons. Nat Neurosci 14, 519–526. doi:10.1038/nn.2767

Peled, E.S., Newman, Z.L., Isacoff, E.Y., 2014. Evoked and spontaneous transmission favored by distinct sets of synapses. Curr Biol 24, 484–493. doi:10.1016/j.cub.2014.01.022

Petersen, S.A., Fetter, R.D., Noordermeer, J.N., Goodman, C.S., DiAntonio, A., 1997. Genetic analysis of glutamate receptors in *Drosophila* reveals a retrograde signal regulating presynaptic transmitter release. Neuron 19, 1237–1248.

Petzoldt, A.G., Lee, Y.H., Khorramshahi, O., Reynolds, E., Plested, A.J., Herzel, H., Sigrist, S.J., 2014. Gating characteristics control glutamate receptor distribution and trafficking *in vivo*. Curr Biol 24, 2059–2065. doi:10.1016/j.cub.2014.07.051

Piccioli, Z.D., Littleton, J.T., 2014. Retrograde BMP signaling modulates rapid activity-dependent synaptic growth via presynaptic LIM kinase regulation of cofilin. J Neurosci 34, 4371–4381. doi:10.1523/JNEUROSCI.4943-13.2014

Qin, G., Schwarz, T., Kittel, R.J., Schmid, A., Rasse, T.M., Kappei, D., Ponimaskin, E., Heckmann, M., Sigrist, S.J., 2005. Four different subunits are essential for expressing the synaptic glutamate receptor at neuromuscular junctions of *Drosophila*. J Neurosci 25, 3209–3218. doi:10.1523/JNEUROSCI.4194-04.2005

Rasse, T.M., Fouquet, W., Schmid, A., Kittel, R.J., Mertel, S., Sigrist, C.B., Schmidt, M., Guzman, A., Merino, C., Qin, G., Quentin, C., Madeo, F.F., Heckmann, M., and Sigrist, S.J., 2005. Glutamate receptor dynamics organizing synapse formation *in vivo*. Nat Neurosci 8, 898–905. doi:10.1038/nn1484

Reddy-Alla, S., Böhme, M.A., Reynolds, E., Beis, C., Grasskamp, A.T., Mampell, M.M., Maglione, M., Jusyte, M., Rey, U., Babikir, H., McCarthy, A.W., Quentin, C., Matkovic, T., Bergeron, D.D., Mushtaq, Z., Göttfert, F., Owald, D., Mielke, T., Hell, S.W., Sigrist, S.J. and Walter, A.M., 2017. Stable positioning of unc13 restricts synaptic vesicle fusion to defined release sites to promote synchronous neurotransmission. Neuron 95, 1350–1364.e12. doi:10.1016/j.neuron.2017.08.016

Reid, C.A., Bekkers, J.M., Clements, J.D., 2003. Presynaptic $Ca^{2+}$ channels: a functional patchwork. Trends Neurosci 26, 683–687. doi:10.1016/j.tins.2003.10.003

Rieckhof, G.E., Yoshihara, M., Guan, Z., Littleton, J.T., 2003. Presynaptic N-type calcium channels regulate synaptic growth. J Biol Chem 278, 41099–41108. doi:10.1074/jbc.M306417200

Ritzenthaler, S., Chiba, A., 2003. Myopodia (postsynaptic filopodia) participate in synaptic target recognition. J Neurobiol 55, 31–40. doi:10.1002/neu.10180

Ritzenthaler, S., Suzuki, E., Chiba, A., 2000. Postsynaptic filopodia in muscle cells interact with innervating motoneuron axons. Nat Neurosci 3, 1012–1017. doi:10.1038/79833

Schikorski, T., Stevens, C.F., 1997. Quantitative ultrastructural analysis of hippocampal excitatory synapses. J Neurosci 17, 5858–5867.

Schmid, A., Hallermann, S., Kittel, R.J., Khorramshahi, O., Frölich, A.M.J., Quentin, C., Rasse, T.M., Mertel, S., Heckmann, M., and Sigrist, S.J., 2008. Activity-dependent site-specific changes of glutamate receptor composition *in vivo*. Nat Neurosci 11, 659–666. doi:10.1038/nn.2122

Schoch, S., Gundelfinger, E.D., 2006. Molecular organization of the presynaptic active zone. Cell Tissue Res 326, 379–391. doi:10.1007/s00441-006-0244-y

Schuster, C.M., Davis, G.W., Fetter, R.D., Goodman, C.S., 1996. Genetic dissection of structural and functional components of synaptic plasticity. I. Fasciclin II controls synaptic stabilization and growth. Neuron 17, 641–654.

Schuster, C.M., Ultsch, A., Schloss, P., Cox, J.A., Schmitt, B., Betz, H., 1991. Molecular cloning of an invertebrate glutamate receptor subunit expressed in *Drosophila* muscle. Science 254, 112–114.

Sheng, J., He, L., Zheng, H., Xue, L., Luo, F., Shin, W., Sun, T., Kuner, T., Yue, D.T., Wu, L.-G., 2012. Calcium-channel number critically influences synaptic strength and plasticity at the active zone. Nat Neurosci 15, 998–1006. doi:10.1038/nn.3129

Sigrist, S.J., Reiff, D.F., Thiel, P.R., Steinert, J.R., Schuster, C.M., 2003. Experience-dependent strengthening of *Drosophila* neuromuscular junctions. J. Neurosci. 23, 6546--6556.

Smith, L.A., Wang, X., Peixoto, A.A., Neumann, E.K., Hall, L.M., Hall, J.C., 1996. A *Drosophila* calcium channel alpha1 subunit gene maps to a genetic locus associated with behavioral and visual defects. J Neurosci 16, 7868–7879.

Stanley, E.F., 2016. The nanophysiology of fast transmitter release. Trends Neurosci 39, 183–197. doi:10.1016/j.tins.2016.01.005

1098 Südhof, T.C., 2012. The presynaptic active zone. Neuron 75, 11–25.
1099 doi:10.1016/j.neuron.2012.06.012

1100 Sugie, A., Hakeda-Suzuki, S., Suzuki, E., Silies, M., Shimozono, M., Möhl, C., Suzuki, T. and
1101 Tavosanis, G., 2015. Molecular Remodeling of the Presynaptic Active Zone of
1102 *Drosophila* Photoreceptors via Activity-Dependent Feedback. Neuron 86, 711–725.
1103 doi:10.1016/j.neuron.2015.03.046

1104 Tang, A.-H., Chen, H., Li, T.P., Metzbower, S.R., MacGillavry, H.D. and Blanpied, T.A., 2016.
1105 A trans-synaptic nanocolumn aligns neurotransmitter release to receptors. Nature 536,
1106 210–214. doi:10.1038/nature19058

1107 Tapia, J.C., Wylie, J.D., Kasthuri, N., Hayworth, K.J., Schalek, R., Berger, D.R., Guatimosim,
1108 C., Seung, H.S., Lichtman, J.W., 2012. Pervasive synaptic branch removal in the
1109 mammalian neuromuscular system at birth. Neuron 74, 816–829.
1110 doi:10.1016/j.neuron.2012.04.017

1111 Tedford, H.W., Zamponi, G.W., 2006. Direct G protein modulation of Cav2 calcium channels.
1112 Pharmacol Rev 58, 837–862. doi:10.1124/pr.58.4.11

1113 Van Vactor, D., Sigrist, S.J., 2017. Presynaptic morphogenesis, active zone organization and
1114 structural plasticity in *Drosophila*. Curr Opin Neurobiol 43, 119–129.
1115 doi:10.1016/j.conb.2017.03.003

1116 Wadel, K., Neher, E., Sakaba, T., 2007. The coupling between synaptic vesicles and $Ca^{2+}$
1117 channels determines fast neurotransmitter release. Neuron 53, 563–575.
1118 doi:10.1016/j.neuron.2007.01.021

1119 Wagh, D.A., Rasse, T.M., Asan, E., Hofbauer, A., Schwenkert, I., Dürrbeck, H., Buchner, S.,
1120 Dabauvalle, M.-C., Schmidt, M., Qin, G., Wichmann, C., Kittel, R., Sigrist, S.J.,
1121 Buchner, E., 2006. Bruchpilot, a protein with homology to ELKS/CAST, is required for
1122 structural integrity and function of synaptic active zones in *Drosophila*. Neuron 49, 833–
1123 844. doi:10.1016/j.neuron.2006.02.008

1124 Wang, L.-Y., Neher, E., Taschenberger, H., 2008. Synaptic vesicles in mature calyx of Held
1125 synapses sense higher nanodomain calcium concentrations during action potential-evoked
1126 glutamate release. J Neurosci 28, 14450–14458. doi:10.1523/JNEUROSCI.4245-08.2008

1127 Wegel, E., Göhler, A., Lagerholm, B.C., Wainman, A., Uphoff, S., Kaufmann, R., Dobbie, I.M.,
1128 2016. Imaging cellular structures in super-resolution with SIM, STED and Localisation
1129 Microscopy: A practical comparison. Sci Rep 6, 27290. doi:10.1038/srep27290

1130 Weyhersmüller, A., Hallermann, S., Wagner, N. and Eilers, J., 2011. Rapid active zone
1131 remodeling during synaptic plasticity. J Neurosci 31, 6041–6052.

doi:10.1523/JNEUROSCI.6698-10.2011

Wojtowicz, J.M., Marin, L., Atwood, H.L., 1994. Activity-induced changes in synaptic release sites at the crayfish neuromuscular junction. J Neurosci 14, 3688–3703.

Yoshihara, M., Adolfsen, B., Galle, K.T., Littleton, J.T., 2005. Retrograde signaling by Syt 4 induces presynaptic release and synapse-specific growth. Science 310, 858–863. doi:10.1126/science.1117541

Yoshihara, M., Adolfsen, B., Littleton, J.T., 2003. Is synaptotagmin the calcium sensor? Curr Opin Neurobiol 13, 315–323.

Yoshihara, M., Littleton, J.T., 2002. Synaptotagmin I functions as a calcium sensor to synchronize neurotransmitter release. Neuron 36, 897–908.

Yu, W., Kawasaki, F., Ordway, R.W., 2011. Activity-dependent interactions of NSF and SNAP at living synapses. Mol Cell Neurosci 47, 19–27. doi:10.1016/j.mcn.2011.02.002

Zamponi, G.W., Snutch, T.P., 1998. Modulation of voltage-dependent calcium channels by G proteins. Curr Opin Neurobiol 8, 351–356.

Zhai, R.G., Bellen, H.J., 2004. The architecture of the active zone in the presynaptic nerve terminal. Physiology (Bethesda) 19, 262–270. doi:10.1152/physiol.00014.2004

Z Zhang, Y., Füger, P., Hannan, S.B., Kern, J.V., Lasky, B. and Rasse, T.M., 2010. In vivo imaging of intact *Drosophila* larvae at sub-cellular resolution. J Vis Exp. doi:10.3791/2249

Zito, K., Parnas, D., Fetter, R.D., Isacoff, E.Y., Goodman, C.S., 1999. Watching a synapse grow: noninvasive confocal imaging of synaptic growth in *Drosophila*. Neuron 22, 719–729.

## Figure Legends

**Figure 1.** High $P_r$ sites correspond to single AZs with elevated levels of BRP. (**A**) Representative images of consecutive evoked release events (green flashes) visualized by expressing myrGCaMP6s in muscle 4. The position of each AZ was determined by expressing GluRIIA-RFP to label the corresponding PSD. Evoked release triggers fusion across different sets of AZs during each stimuli, but a subpopulation of AZs respond more frequently (arrow). (**B**) Histogram of the distribution of AZ $P_r$ for a 0.3 Hz 5-minute stimulation paradigm. AZs classified as high $P_r$ (>2 standard deviations above the mean) are shown in red. The percentage of AZs that were low $P_r$ (65.8%), high $P_r$ (9.9%), spontaneous-only (9.7%) and silent (14.6%) is displayed in the inset. (**C**) Average $P_r$ determined for each individual experiment for the AZ population categorized based on low and high activity sites (>2 standard deviations above the mean). Each point represents the average for all AZs (classified as either high or low $P_r$) from a single animal. (**D**) Individual BRP puncta for three NMJs from three different animals imaged with high resolution structured illumination microscopy (SIM, left panel) or confocal microscopy (middle panel). The right panel displays the heat map for evoked $P_r$ from the same NMJs determined by GCaMP6s imaging prior to fixation. Representative high $P_r$ sites are circled with red in the middle panels. The far right top panel displays the results from the automated detection algorithm that outlines individual AZs. (**E**) AZs were separated into high and low $P_r$ based on their activity and the fluorescence intensity of the corresponding BRP puncta is shown (from conventional confocal images). (**F**) AZs with high BRP intensity (two standard deviations above average) were preselected from conventional confocal images and identified on corresponding SIM images. In cases where the BRP signal was resolvable into more than one AZ by SIM microscopy, it was assigned to the AZ cluster group. In cases where the BRP signal mapped to a

1177 single BRP puncta by SIM imaging, it was assigned to the single AZ group. $P_r$ is plotted for each
1178 group. Student's t-test was used for statistical analysis (*** = p≤0.001). Error bars represent
1179 SEM.

1180

1181 **Figure 2.** Stability of release maps at the NMJ. (**A**) $P_r$ heatmaps for the same muscle 4 NMJ
1182 were generated for two individual imaging sessions, separated by a 5-minute resting period. High
1183 $P_r$ AZs were numbered and re-identified in each heatmap. Representative high $P_r$ AZs that
1184 sustain release rates during the second imaging session are noted with arrows. (**B**) Correlation of
1185 AZ $P_r$ between two imaging sessions separated by a 5-minute resting period. (**C**) $P_r$ heatmaps for
1186 the same NMJ separated by a 5-minute 5 Hz stimulation. Representative high $P_r$ AZs that did not
1187 change activity levels are noted with arrows. (**D**) Correlation of AZ $P_r$ between two imaging
1188 sessions separated by a 5-minute 5 Hz stimulation period.

1189

1190 **Figure 3.** $P_r$ variability remains in *syt1* null mutants. (**A**) The left panel displays the distribution
1191 of GluRIIA staining in *syt1* nulls (left panel) at the muscle 4 NMJ. The corresponding $P_r$
1192 heatmap is shown on the right. The arrows denote several high $P_r$ sites opposed by bright
1193 GluRIIA positive PSDs. (**B**) AZ release events per second for spontaneous release and evoked by
1194 5 Hz stimulation are shown for *syt1* nulls mutants, and for spontaneous release in controls. (**C**)
1195 Frequency distribution of $P_r$ is shown for *syt1* nulls and controls. (**D**) Plot of normalized $P_r$
1196 frequency distribution (from 0 to 1 (max)) for *syt1* nulls and controls. (**E**) Cumulative frequency
1197 distribution for normalized release rates for *syt1* nulls and controls is shown. Student's t-test was
1198 used for statistical analysis (*** = p≤0.001). Error bars represent SEM.

**Figure 4**. $P_r$ correlates with Cac channel density at AZs. (**A**) Representative images showing heterogeneous distribution of Cac-TdTomato at the NMJ of muscle 4 (left panel). Evoked release was visualized at the same NMJ using myrGCaMP6s (second panel) and AZ release maps were generated for evoked (third panel) and spontaneous fusion (right panel). Several high $P_r$ AZs with bright Cac density are noted (arrows). (**B**) Correlation between AZ $P_r$ and Cac-TdTomato fluorescent intensity for evoked release. (**C**). Correlation between AZ spontaneous release rate per second and Cac-TdTomato fluorescence intensity. (**D**) Representative images showing heterogeneous distribution of Cac-GFP at the NMJ (left panel). Evoked release visualized at the same NMJ by myr-jRGECO is shown in the second panel. The $P_r$ heatmap for evoked release is shown in the third panel. A heatmap distribution of Cac-GFP fluorescence intensities, based on same criteria as color-coding of $P_r$, is shown in the right panel. The arrows denote several higher $P_r$ sites containing bright Cac-GFP puncta. (**E**) Correlation between AZ $P_r$ and Cac-GFP fluorescence intensity for evoked release. (**F**) Cac-GFP fluorescence obtained for AZs functionally classified as either low or high $P_r$ (>2 standard deviations above mean) by quantal imaging with myr-jRGECO1a. Student's t-test was used for statistical analysis (*** = $p \leq 0.001$). Error bars represent SEM.

**Figure 5.** GCaMP-BRP detects relative $Ca^{2+}$ influx at single AZs and is correlated with Cac channel density. (**A**) Representative images of the same muscle 4 NMJ bouton showing CCaMP6m-BRP fluorescence at rest and following 10 Hz stimulation for two consecutive rounds. (**B**) The AZ fluorescence intensity was plotted for three independent rounds of

1221 stimulation for BRP-GCaMP6m. Fluorescence changes per AZ remain stable for the same AZ
1222 during multiple rounds of stimulation. (**C**) Histogram of the distribution of relative fluorescence
1223 intensities (ΔF) across AZs for BRP-GCaMP6m. (**D**) Representative images showing
1224 GCaMP6m-BRP fluorescence before (left panel) and during stimulation (middle panel). The
1225 corresponding distribution of Cac channels labeled by Cac-TdTomato is shown for the same
1226 NMJ (right panel). Examples of rare Cac-positive AZs that showed no corresponding $Ca^{2+}$ influx
1227 are indicated (arrows). (**E**) Correlation between GCaMP6m-BRP ΔF during stimulation and Cac-
1228 TdTomato fluorescence intensity at individual AZs.

1229

1230 **Figure 6.** $P_r$ correlates with the relative levels of $Ca^{2+}$ influx at AZs. (**A**) Two representative
1231 muscle 4 NMJs with AZ $P_r$ heatmaps obtained following myr-jRGECO mapping during
1232 stimulation (left panel). GCaMP6m-BRP fluorescence levels of the same NMJ at rest (second
1233 panel) and during stimulation (third panel) are shown. Heatmaps of GCaMP6m-BRP ΔF during
1234 stimulation are displayed in the right panel. Several representative high $P_r$ AZs that experienced
1235 the strongest $Ca^{2+}$ influx detected by GCaMP-BRP are noted (arrows). (**B**) Correlation between
1236 GCaMP6m-BRP ΔF (during 10 Hz stimulation) and AZ $P_r$ (during 1 Hz stimulation) is shown
1237 across all experiments. (**C**) Representative correlation between GCaMP6m-BRP ΔF and AZ
1238 release rate per minute for evoked (red) and spontaneous (green) fusion for a representative
1239 single NMJ.

1240

1241 **Figure 7.** High $P_r$ AZs have elevated PSD GluRIIA levels and display a distinct pattern of
1242 glutamate receptor clustering. (**A**) Representative image showing the heterogeneous distribution

of GluRIIA-RFP (left panel) at a 3rd instar muscle 4 NMJ. More uniform GluRIIB-GFP PSD puncta can also be observed over the much dimmer myrGCaMP6s (second panel). BRP distribution (third panel) and $P_r$ heatmaps (right panel) for the same NMJ are shown. The correlation between AZ $P_r$ and GluRIIA-RFP (**B**), GluRIIB (**C**) and BRP (**D**) fluorescence intensity is plotted. (**E**) Representative images showing distribution of GluRIIA, GluRIIB and BRP, without co-expression of myrGCaMP6s. Synapses containing bright GluRIIA puncta have GluRIIB predominantly localized to the periphery of the PSD (arrows), surrounding a GluRIIA core. These AZs have higher BRP intensities as well. (**F**) Fluorescence line profiles showing GluRIIA, GluRIIB and BRP normalized fluorescence distribution across individual AZs. All AZs were separated into two groups according to their GluRIIA brightness, with "bright" PSDs based on their GluRIIA intensity (2 standard deviations above average). The peripheral distribution of GluRIIB around central GluRIIA cores was only obvious for bright GluRIIA-positive PSDs that were shown to be more active during stimulation. Correlation between GluRIIA-RFP (**G**) or GluRIIB-GFP (**H**) with BRP intensity at individual AZs.

**Figure 8.** Glutamate receptor segregation during PSD development. **(A)** Two representative muscle 26 NMJs visualized during live imaging in early 1st instar larvae expressing GluRIIA-RFP and GluRIIB-GFP. The arrows denote GluRIIA-RFP positive extensions from the main arbor that are devoid of detectable PSDs or GluRIIB at this stage of development. These extensions disappear during imaging from later larval stages, but some go on to develop fully formed synaptic boutons with new AZs (Figure 8 - supplemental figure 3). (**B**) Representative serial time points of NMJ development visualized by repeated imaging through the cuticle of an anesthetized larvae at the indicated time points beginning at the early 1st instar stage. Two of the

1266 five PSDs present during the first imaging session are labeled and are the first to develop the
1267 peripheral GluRIIB segregation pattern 36 hours later. GluRIIB labeling alone is shown in the
1268 bottom panel. The right panels show GluRIIB fluorescence and normalized GluRIIA and
1269 GluRIIB fluorescent line profiles for the indicated PSDs at the initial imaging session (0 hour)
1270 and 36 hours later. (**C**) Serial images of an NMJ with a larger number of AZs present at the 1st
1271 instar stage. After 36 hours of development, the peripheral segregation of GluRIIB around
1272 GluRIIA was first observed at PSDs that were present during the initial imaging session
1273 (numbered). The right panels show GluRIIB fluorescence and normalized GluRIIA and GluRIIB
1274 fluorescent line profiles for the indicated PSDs at the initial imaging session (0 hour) and 36
1275 hours later. The dashed box surrounds the actual imaged segment of the NMJ in each panel.

1276

1277 **Figure 9.** Rate of acquisition of glutamate receptor segregation during development. Histograms
1278 of the distribution of normalized GluRIIA and GluRIIB fluorescence at the 1st instar (day 1) (**A**)
1279 and 3rd instar (day 4) (**B**) stages for muscle 26 imaged through the cuticle of anesthetized larvae.
1280 For each data set, GluRIIA and GluRIIB fluorescence is presented from dimmest (0) to brightest
1281 (1). GluRIIA shows a more skewed distribution of fluorescence at day 4, consistent with its
1282 accumulation at high $P_r$ AZs. (**C**) Representative muscle 26 NMJ image sequence showing
1283 appearance and maturation of two new synapses (#3 and 4) that were not present in the initial
1284 imaging session. Several preexisting synapses (#1 and 2) that developed the typical GluRIIB
1285 donut structure later in development are also labeled. The dashed box surrounds the actual
1286 imaged segment of the NMJ. New GluRIIA and GluRIIB clusters appear initially as small puncta
1287 (day 2, arrows) that become brighter on day 3. By day 4 they begin to display the donut like
1288 GluRIIB profile. At day 5, GluRIIB distribution to the periphery around a bright GluRIIA PSD

representative of high $P_r$ sites becomes prominent. The bottom panels show normalized GluRIIA and GluRIIB fluorescent line profiles for the newly identified PSDs (#3, 4) throughout the 5 day imaging series. (**D**) Changes in AZ number during larval maturation at muscle 26 presented as a ratio of AZs observed during the first day of imaging (day 1).

## Supplemental Figure Legends

**Figure 4 - supplemental figure 1.** Cac-GFP distribution at AZs analyzed by SIM microscopy. (**A**) Representative Cac-GFP and BRP puncta at AZs for two synaptic boutons imaged using SIM microscopy. (**B**) Histogram of the distribution of mean Cac-GFP fluorescence intensity across the AZ population. Red corresponds to the Cac-GFP containing AZ population with fluorescence intensity 2 standard deviations above the mean. (**C**) Mean fluorescence intensity of Cac-GFP for bright (fluorescence greater than 2 standard deviations above the average) versus dim AZs. Student's t-test was used for statistical analysis (*** = $p \leq 0.001$). Error bars represent SEM.

**Figure 7 - supplemental figure 1.** Correlation between GluRIIA and Cac fluorescence intensities during early larval development. (**A**) Representative Cac-GFP (green) and GluRIIA-RFP (red) synaptic puncta at a muscle 26 NMJ imaged through the cuticle of an anesthetized animal during early larval development. Arrows denote AZs with bright Cac-GFP opposed to PSDs with high levels of GluRIIA. (**B**) Correlation between GluRIIA-RFP and Cac-GFP at individual AZs.

**Figure 8 - supplemental figure 1.** Consecutive imaging of NMJ growth at muscle 26 over a 5-day period imaged through the cuticle of an anesthetized larva during development. The entire NMJ is shown on the left panel. A smaller area (dashed box) is magnified and shown in the right panels. The merged image of GluRIIA and GluRIIB is shown in the middle, with individual GluRIIB and GluRIIA channels on the right. Several PSDs are numbered for tracking across imaging sessions. New PSDs appearing on day 2 (arrow) form the GluRIIB donut by day 4. On day 5, a larger number of PSDs display the characteristic GluRIIB peripheral segregation around a GluRIIA core, including those identified on the 1$^{st}$ day of imaging (numbered).

**Figure 8 - supplemental figure 2.** GluRIIA fluorescence intensity increases over time in a rate proportional to PSD birthdate. Representative serial images of muscle 26 NMJs visualized through the cuticle of two anesthetized larvae during development (**A**, **B**). The dashed box surrounds the actual imaged segment of the NMJ in each panel. The brightest GluRIIA puncta are numbered and followed through the imaging period. The brightest GluRIIA puncta observed on day 1 were among the brightest puncta on later days. Rarely, formation of new PSDs that showed a faster rate of GluRIIA accumulation were observed (arrow). (**C**) By day 5 of larval development, many PSDs show the donut-like GluRIIB distribution, though the number of smaller GluRIIB puncta also increase due to new AZ addition.

**Figure 8 - supplemental figure 3.** Synapse development along early GluRIIA positive NMJ extensions. (**A**) The two representative muscle 26 NMJs shown in Figure 8A were followed

during development. The top panels display the NMJ structure visualized during live imaging in early 1st instar larvae expressing GluRIIA-RFP and GluRIIB-GFP. The GluRIIA-RFP positive extensions from the main arbor that were devoid of detectable PSDs or GluRIIB at this stage of development (large arrow) later formed normal boutons with many PSDs by day 2 and 3. Smaller arrows denote the same PSD at each day for orientation.

**Movie 1**

Representative movie showing evoked and spontaneous GCaMP6s events (green) in larvae expressing GluRIIA-RFP (red) that were stimulated at 0.3 Hz.

**Movie 2**

Representative movie showing spontaneous GCaMP6s events in *syt1* mutants expressing GluRIIA-RFP (red), followed by GCaMP6s events observed during 5 Hz stimulation.

**Movie 3**

Representative movie showing evoked and spontaneous jRGECO events (red) in larvae expressing Cac-GFP (green).

Figure 1



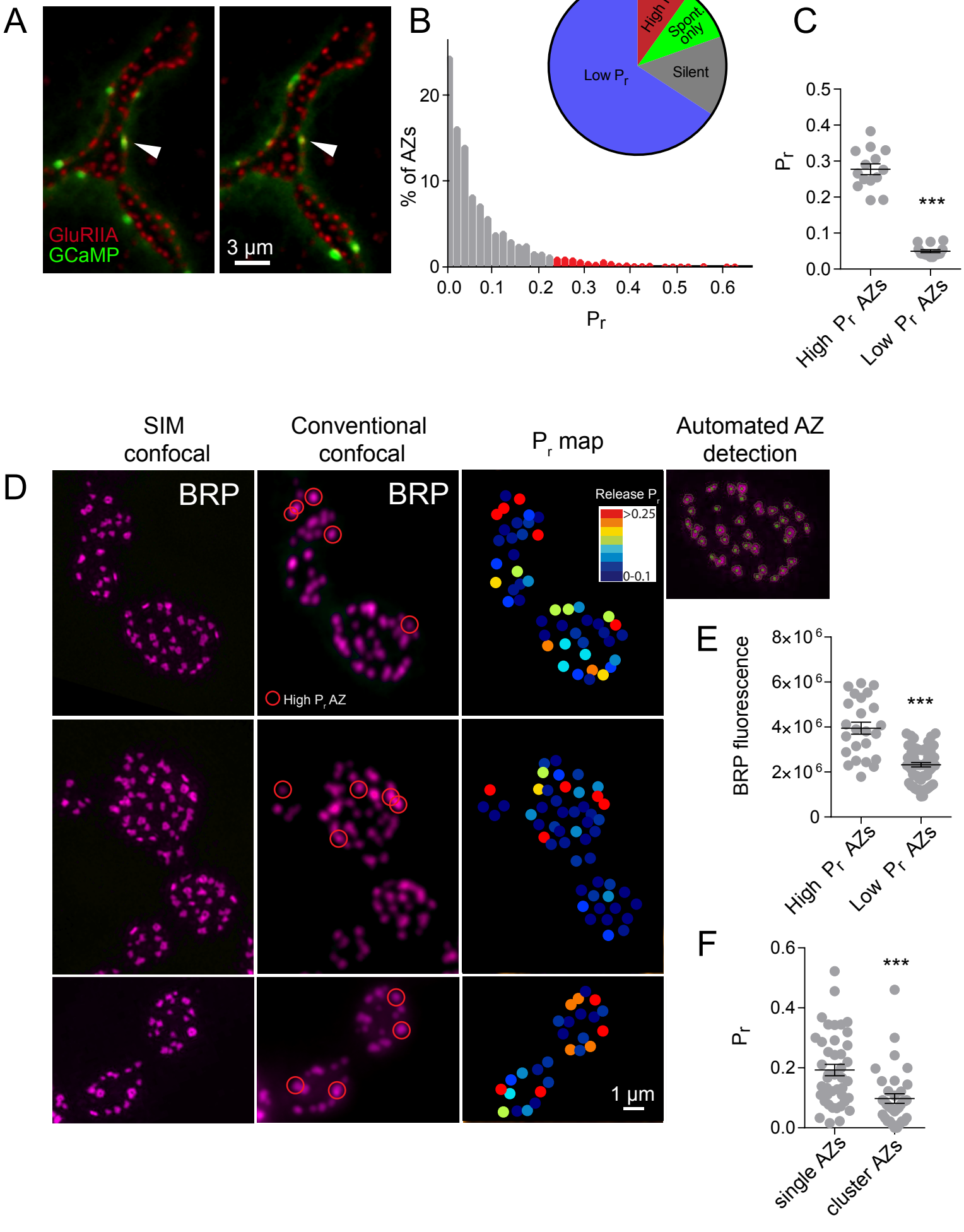

Figure 2

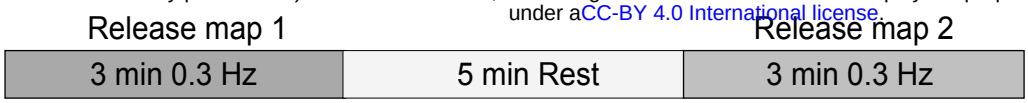


A

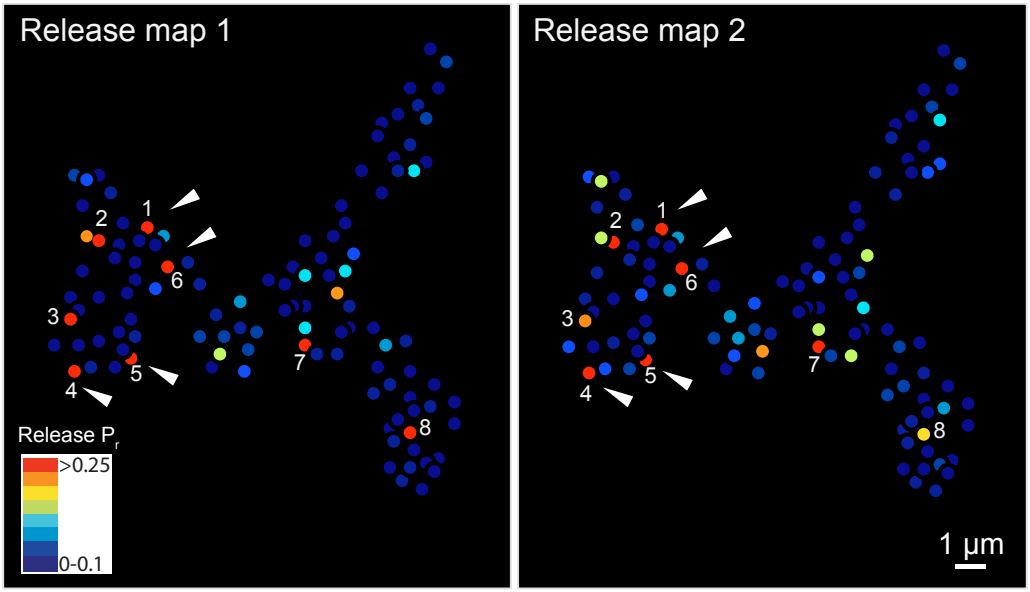


B

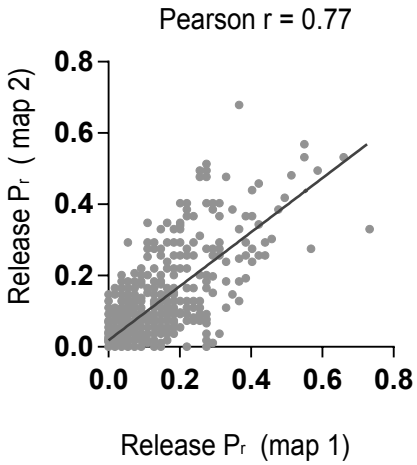


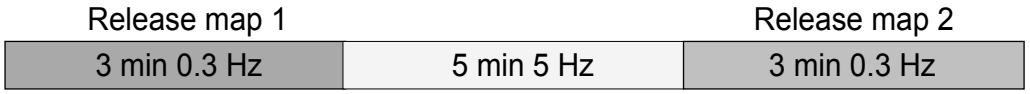


C

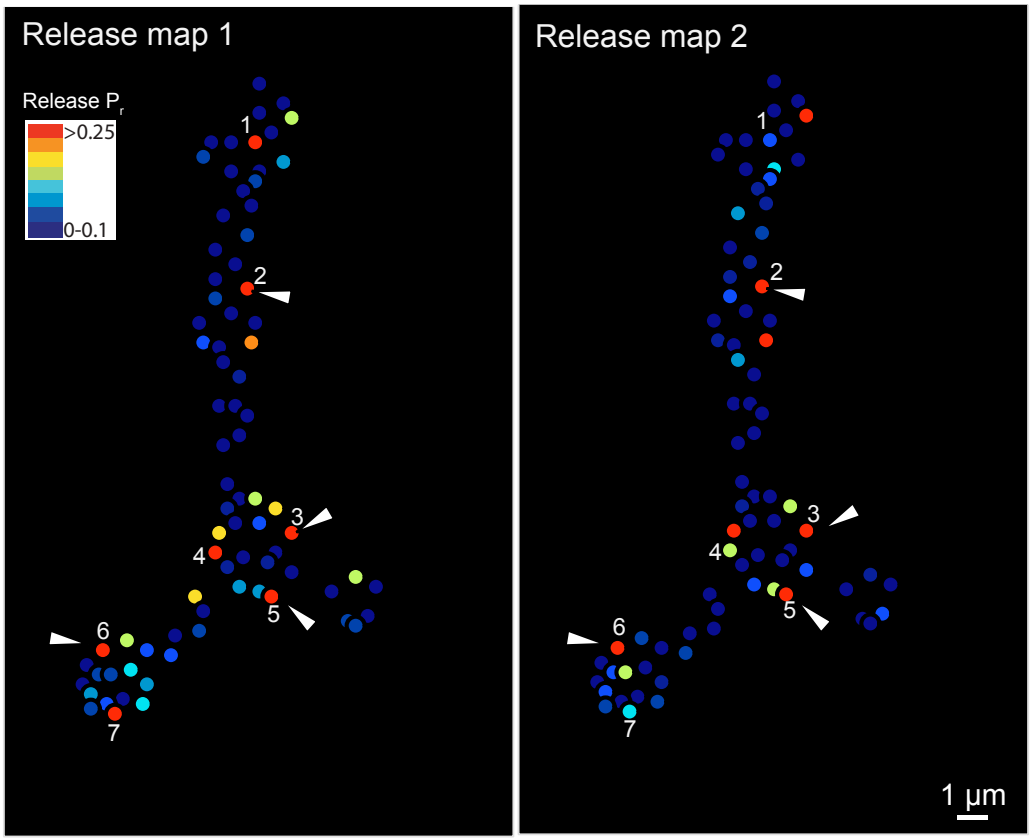


D

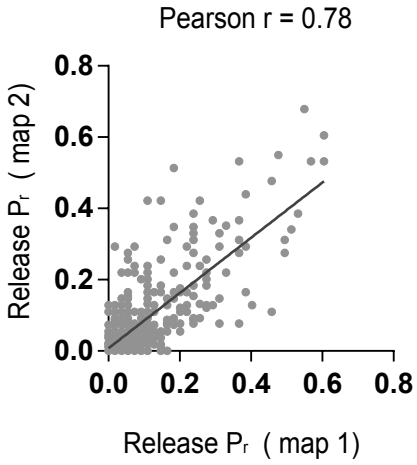

Figure 3



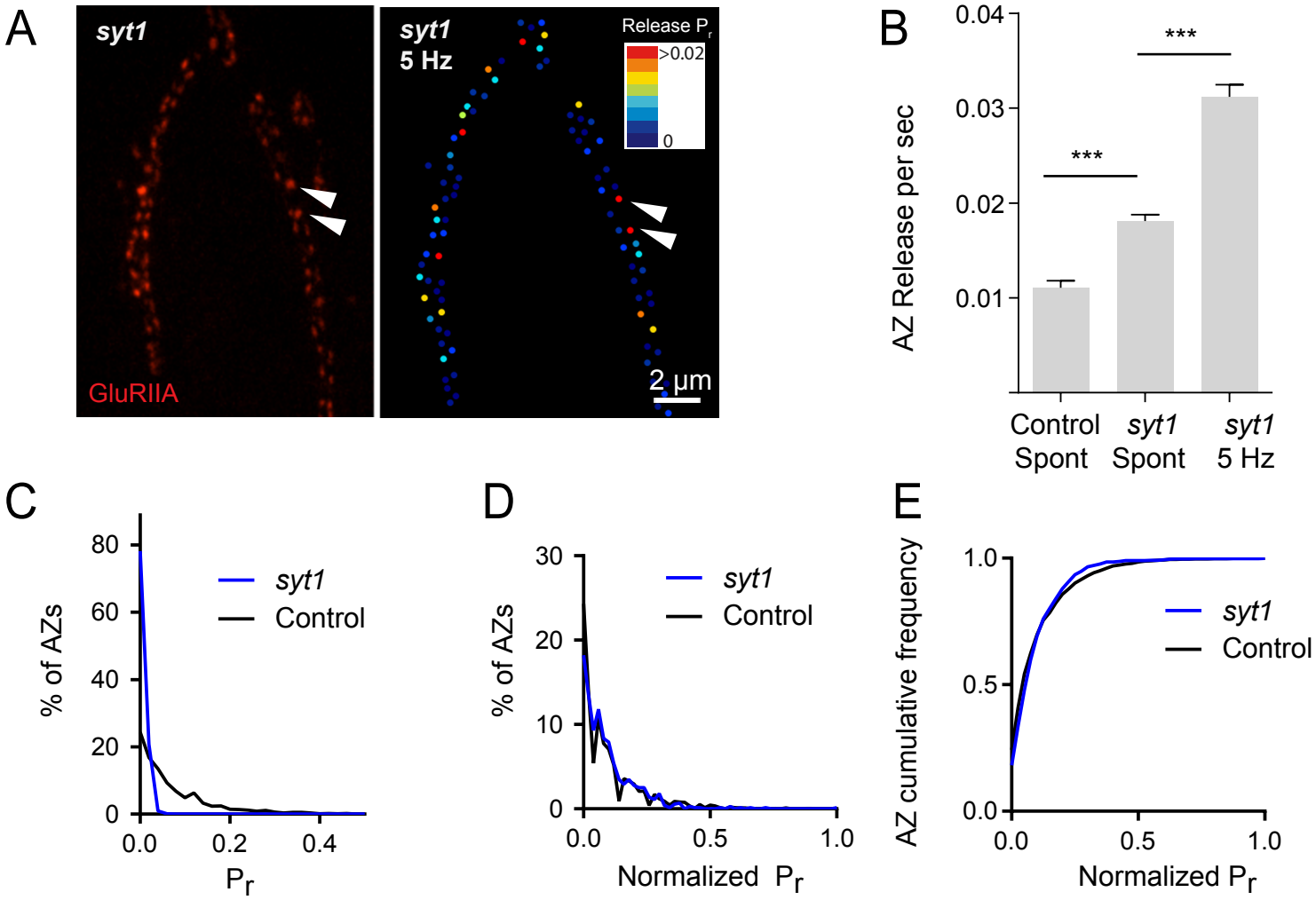

Figure 4



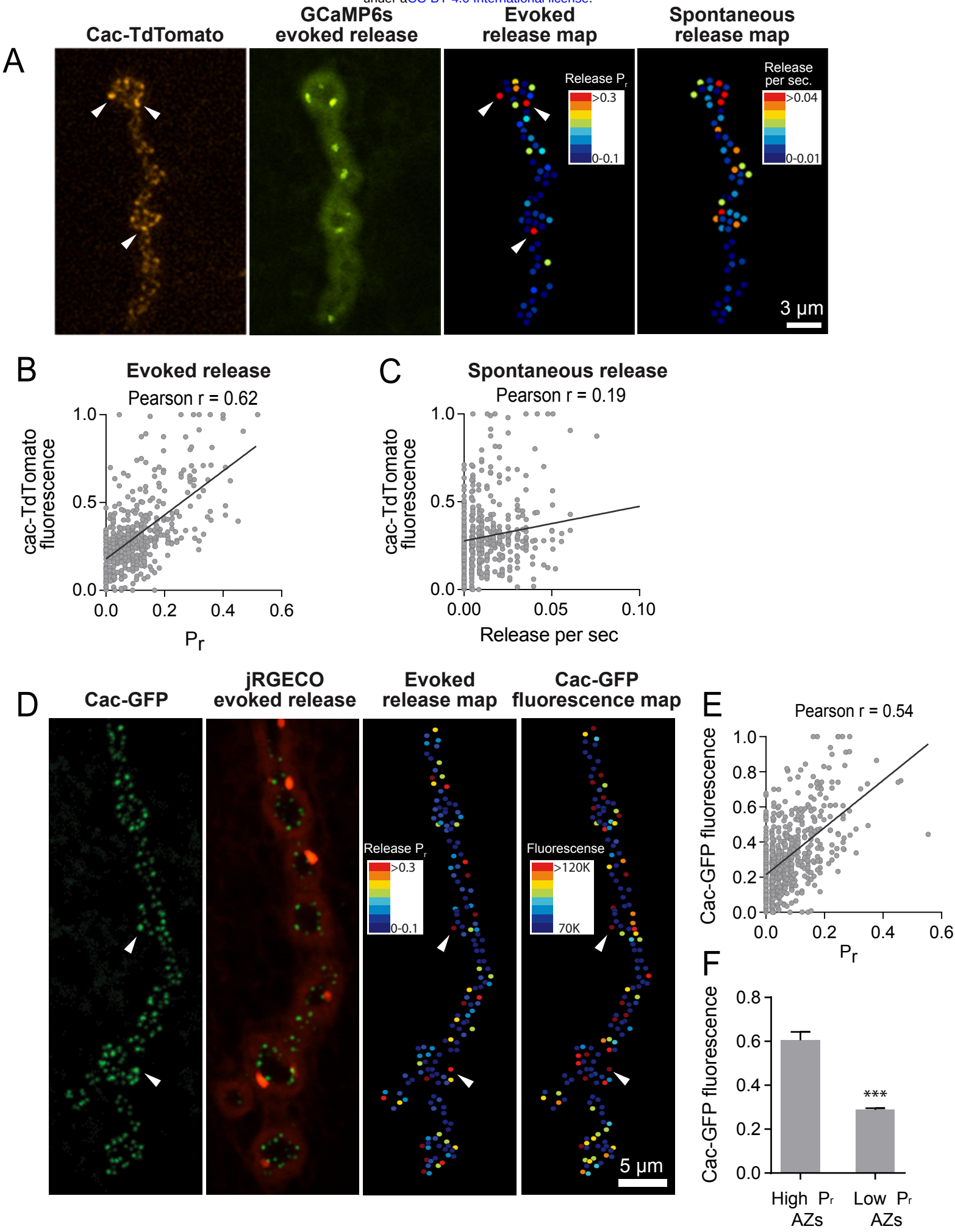

Figure 5

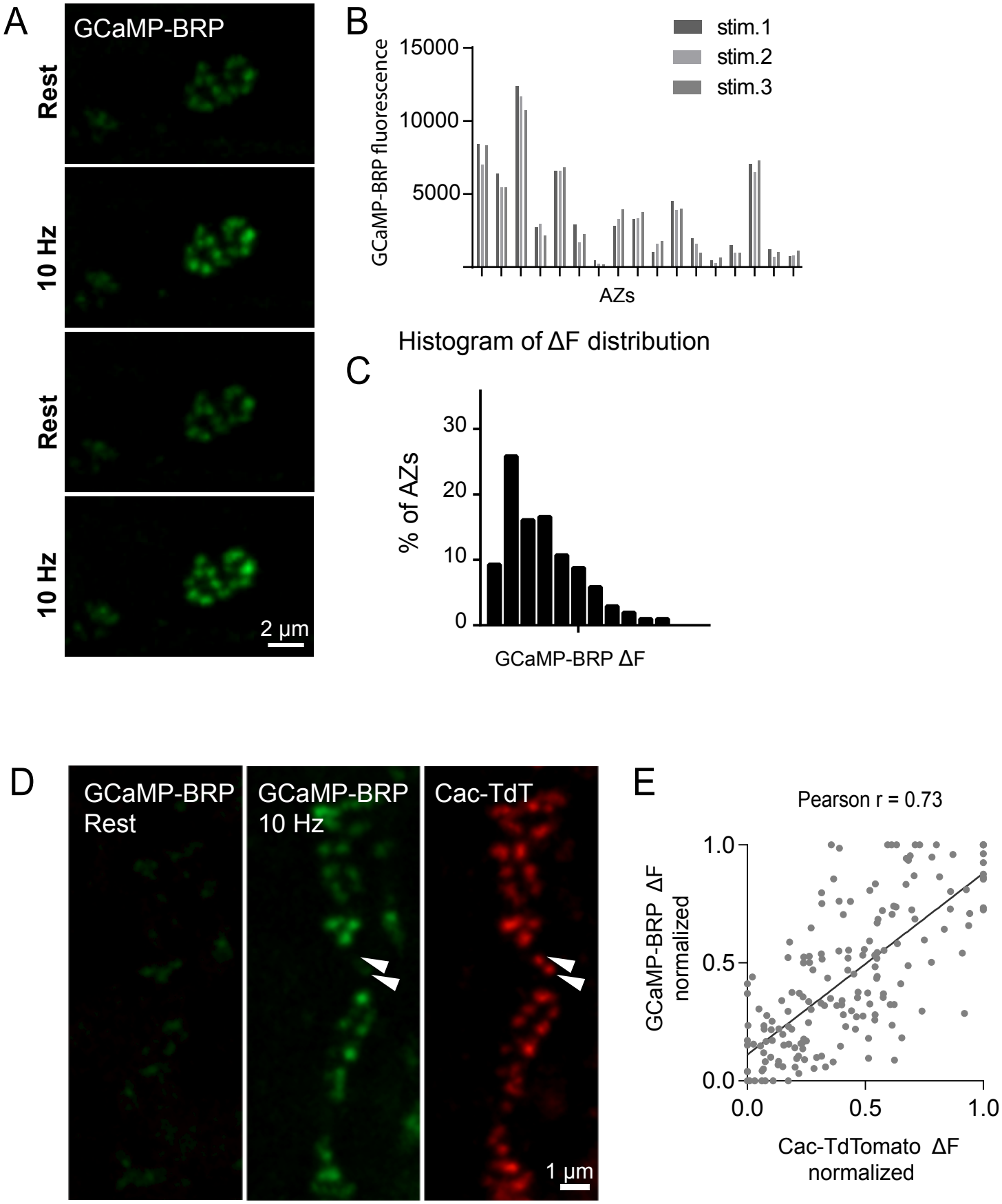

Figure 6



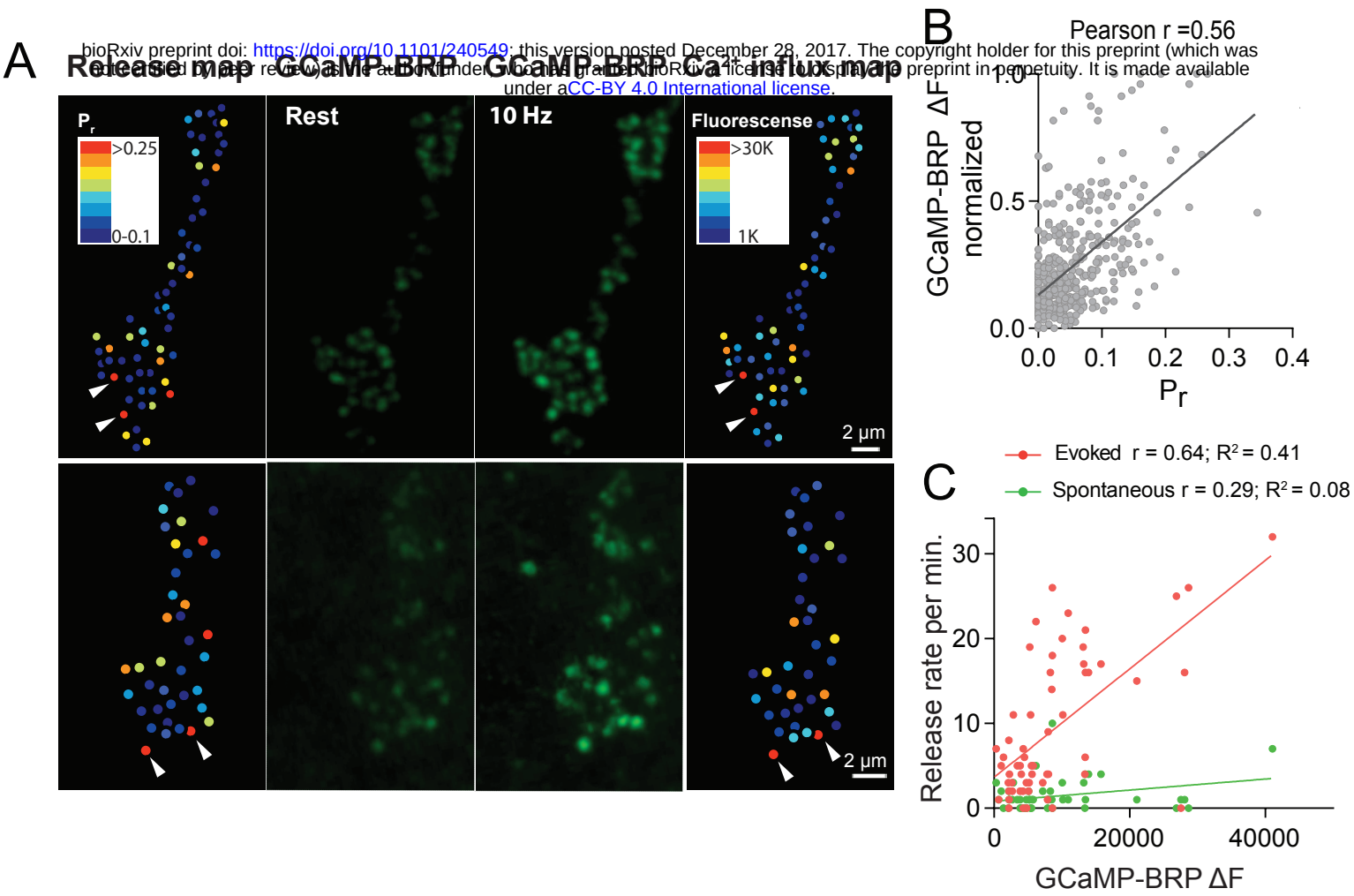

Figure 7

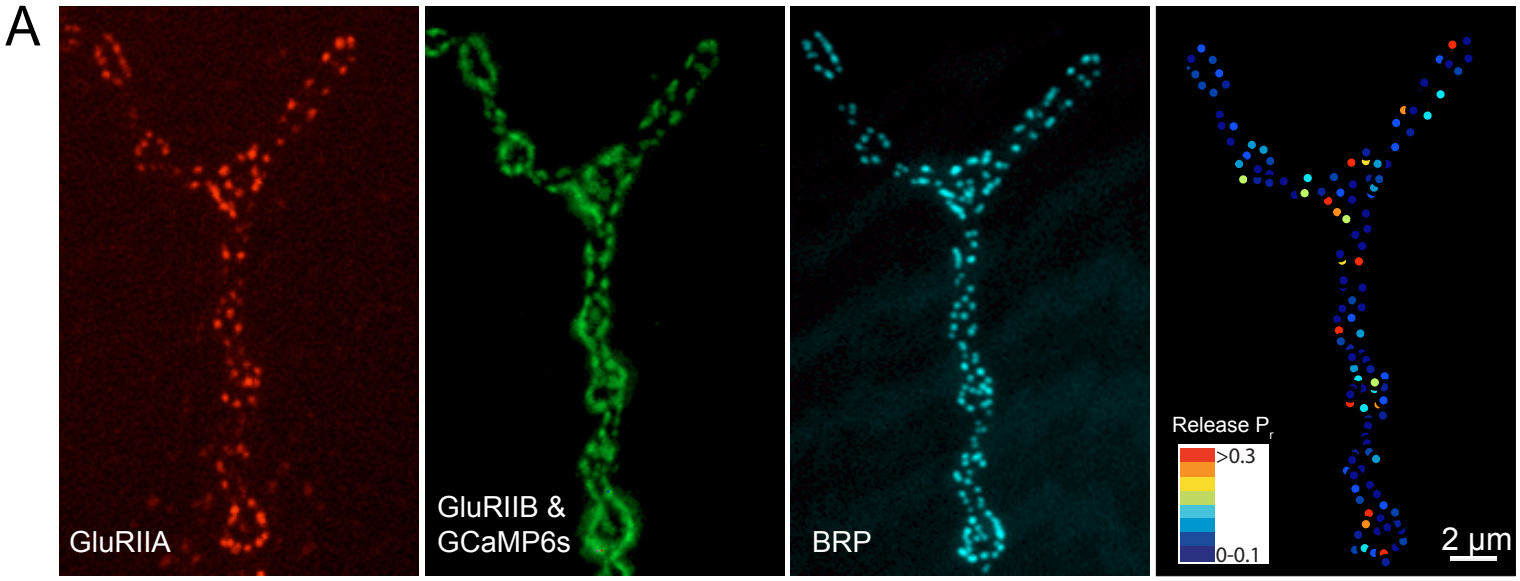


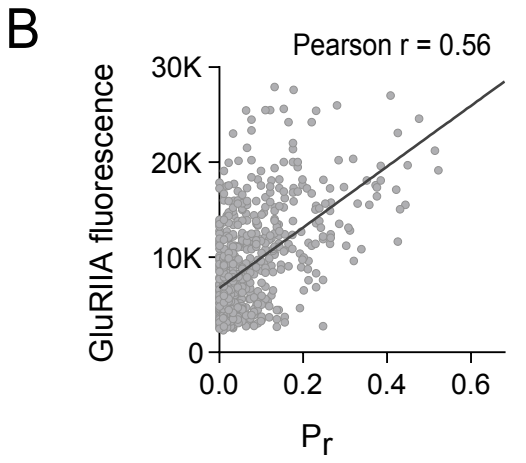


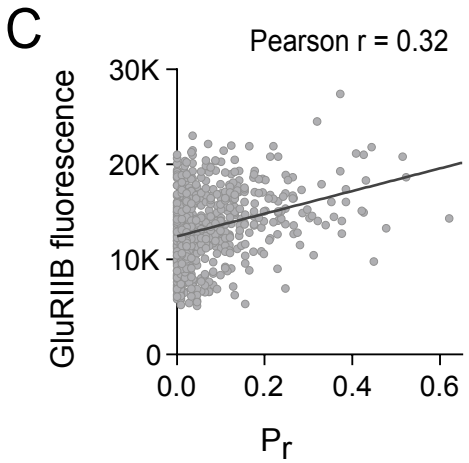


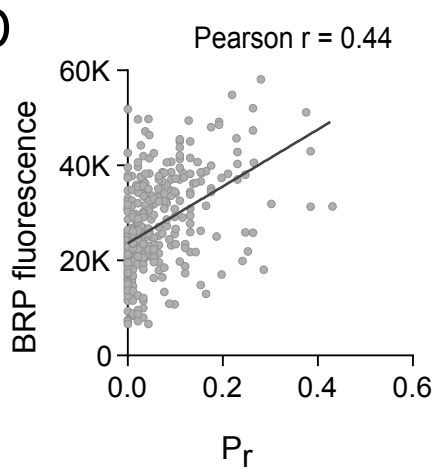


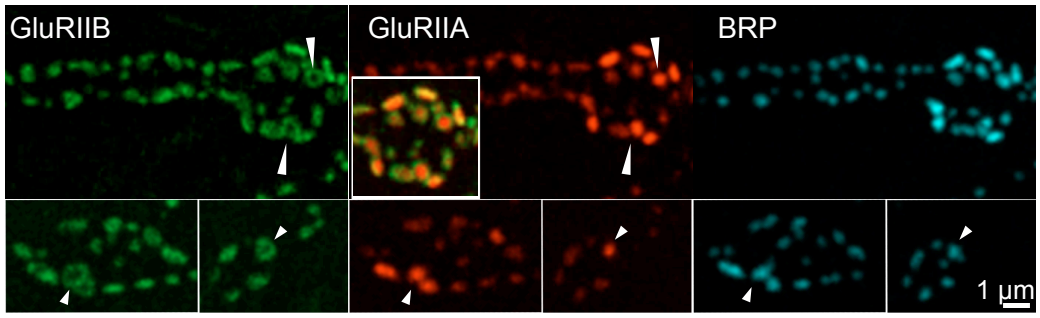


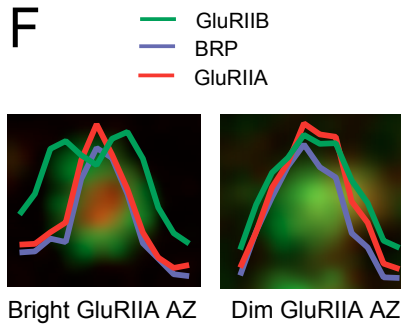


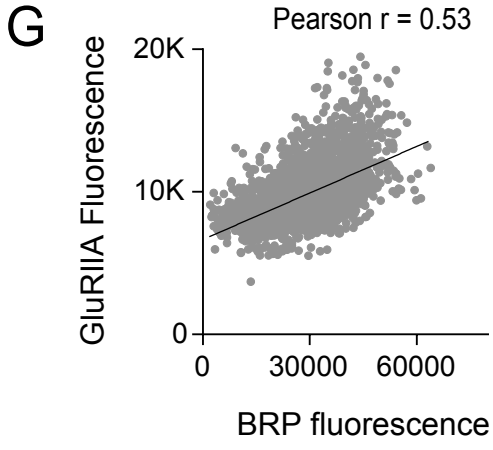


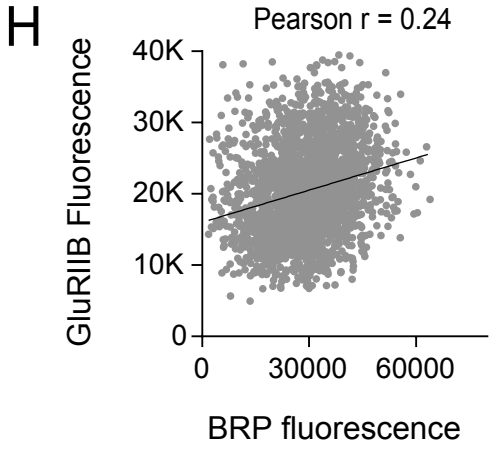

Figure 8

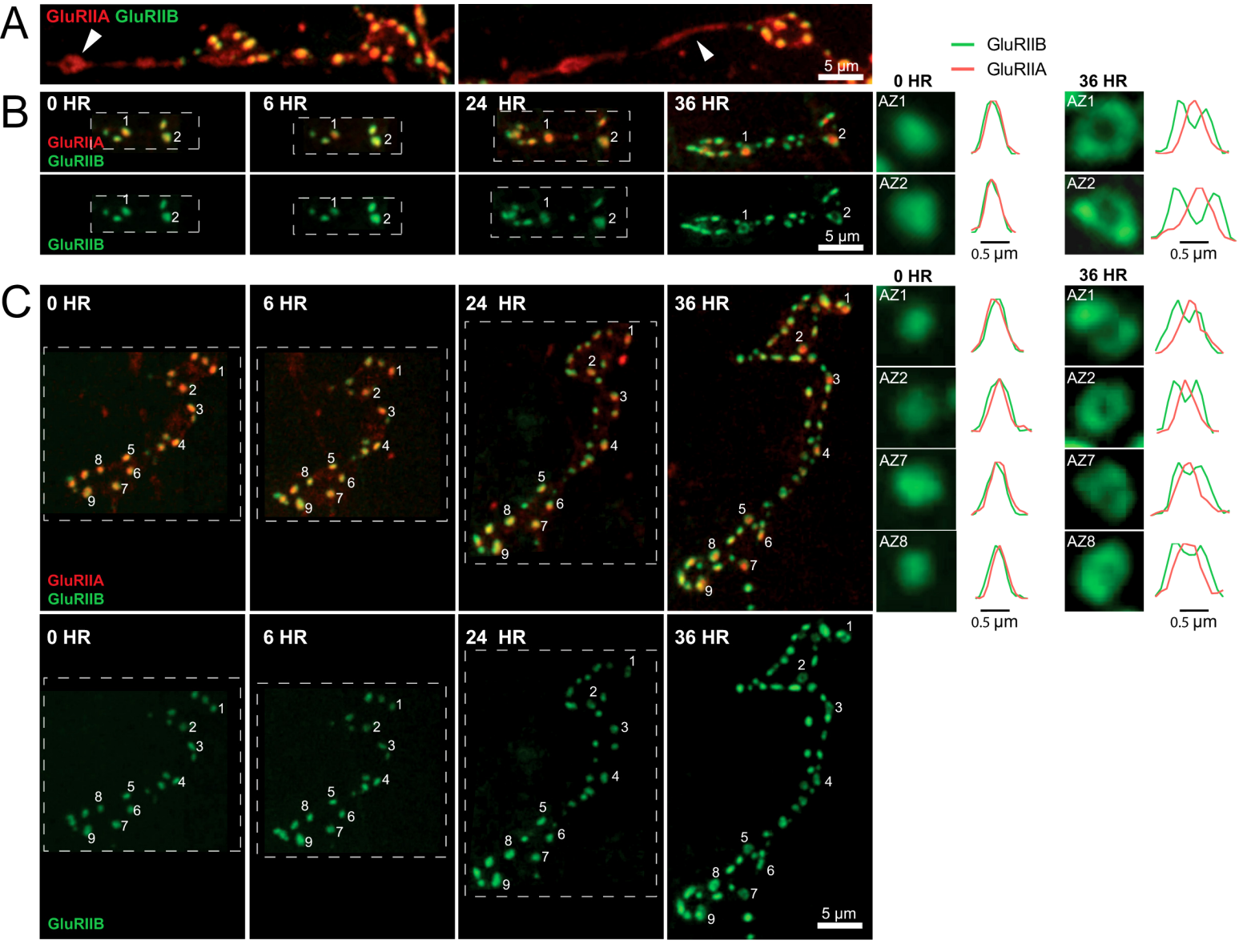
A
GluRIIA GluRIIB
5 µm
B
0 HR
6 HR
24 HR
36 HR
GluRIIA
GluRIIB
GluRIIB
5 µm
GluRIIB
GluRIIA
0 HR
36 HR
AZ1
AZ2
0.5 µm
C
0 HR
6 HR
24 HR
36 HR
GluRIIA
GluRIIB
GluRIIB
5 µm
AZ1
AZ2
AZ7
AZ8
0.5 µm

Figure 9

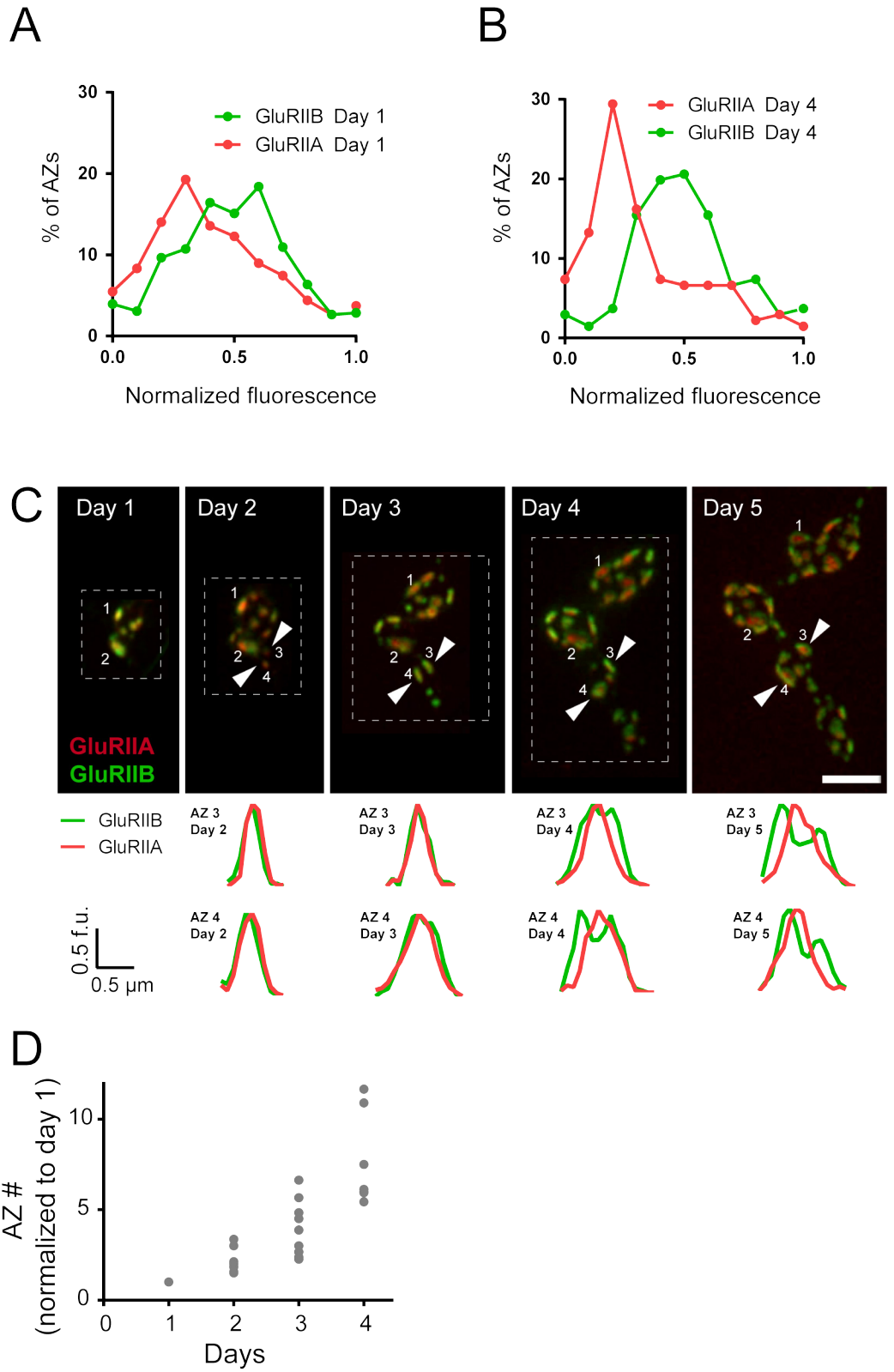
A
30
20
10
0
% of AZs
GluRIIB Day 1
GluRIIA Day 1
0.0
0.5
1.0
Normalized fluorescence
B
30
20
10
0
% of AZs
GluRIIA Day 4
GluRIIB Day 4
0.0
0.5
1.0
Normalized fluorescence
C
Day 1
Day 2
Day 3
Day 4
Day 5
GluRIIA
GluRIIB
GluRIIB
GluRIIA
AZ 3 Day 2
AZ 3 Day 3
AZ 3 Day 4
AZ 3 Day 5
AZ 4 Day 2
AZ 4 Day 3
AZ 4 Day 4
AZ 4 Day 5
0.5 f.u.
0.5 µm
D
AZ # (normalized to day 1)
10
5
0
0
1
2
3
4
Days

# Figure 4- figure supplement 1



A

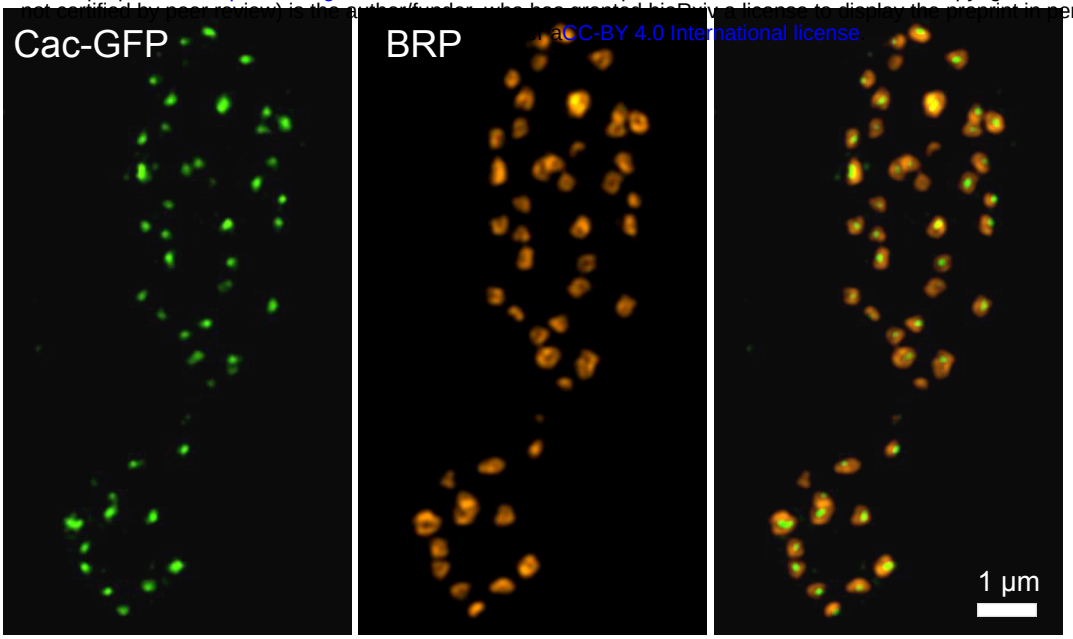


B

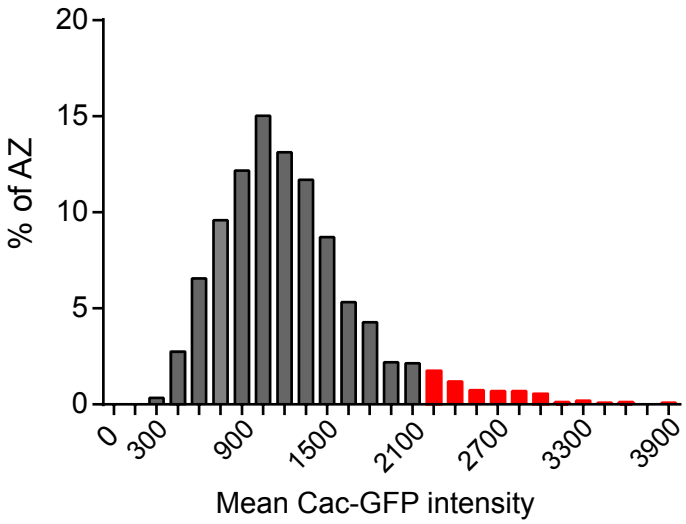


C

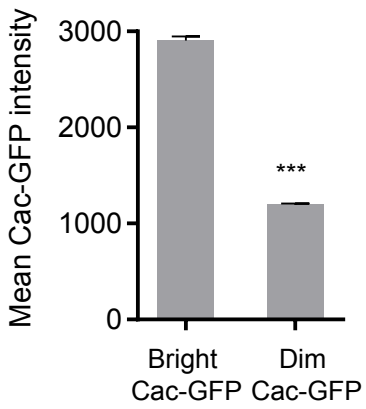

Figure 7 - figure supplement 1



A

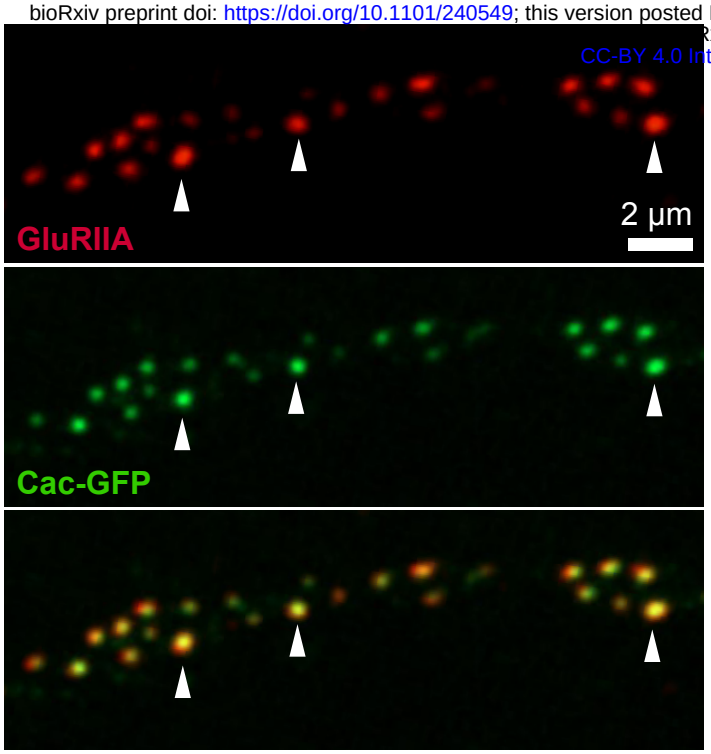


B

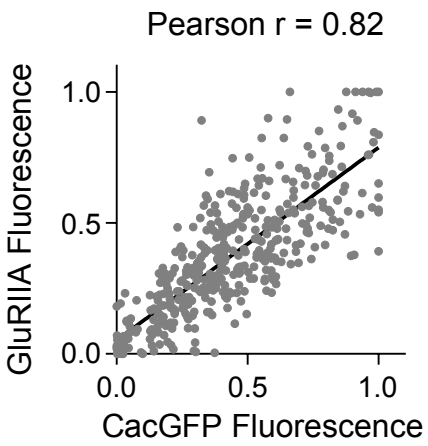

Figure 8 - figure supplement 1

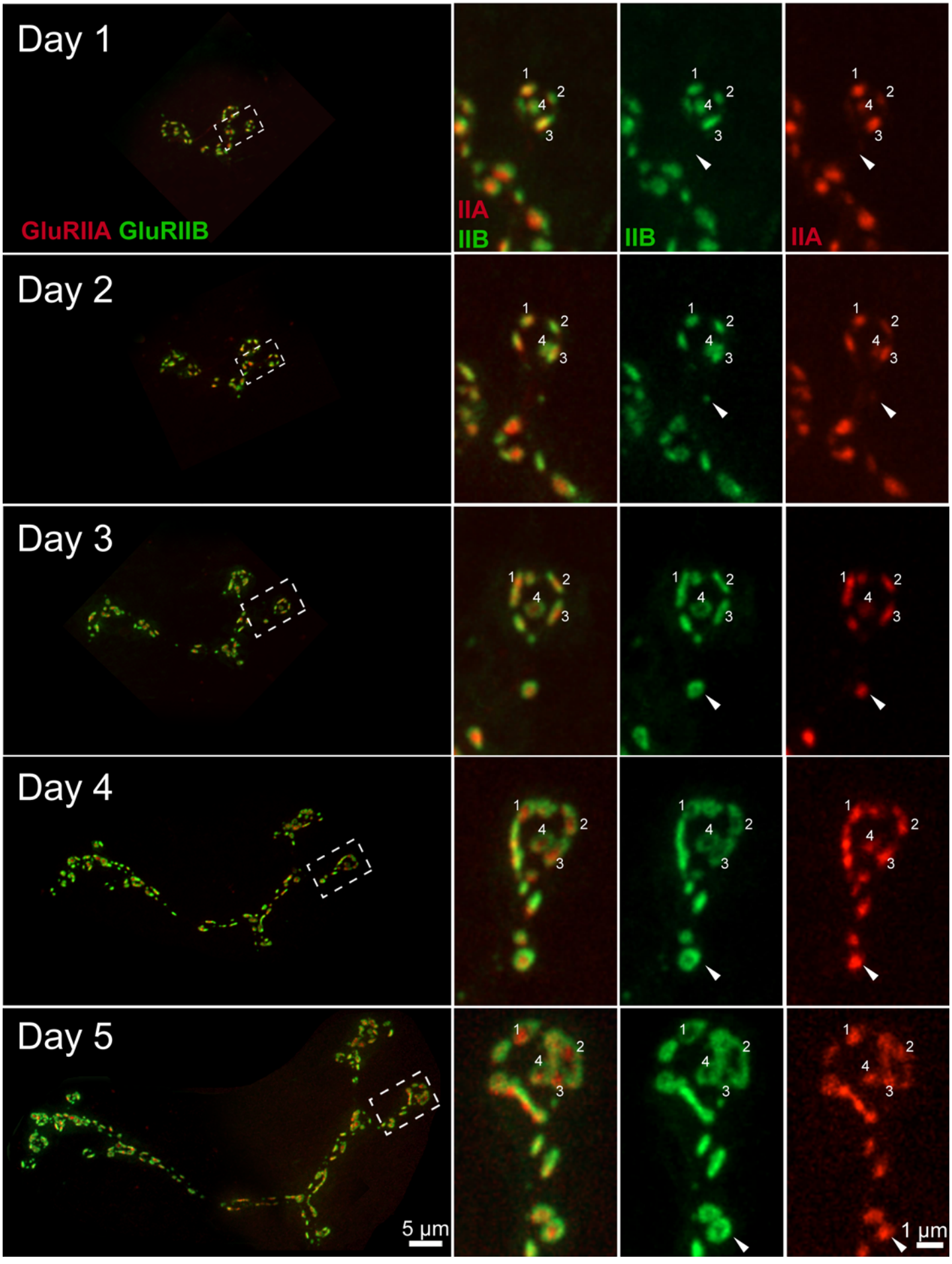

Figure 8 - figure supplement 2

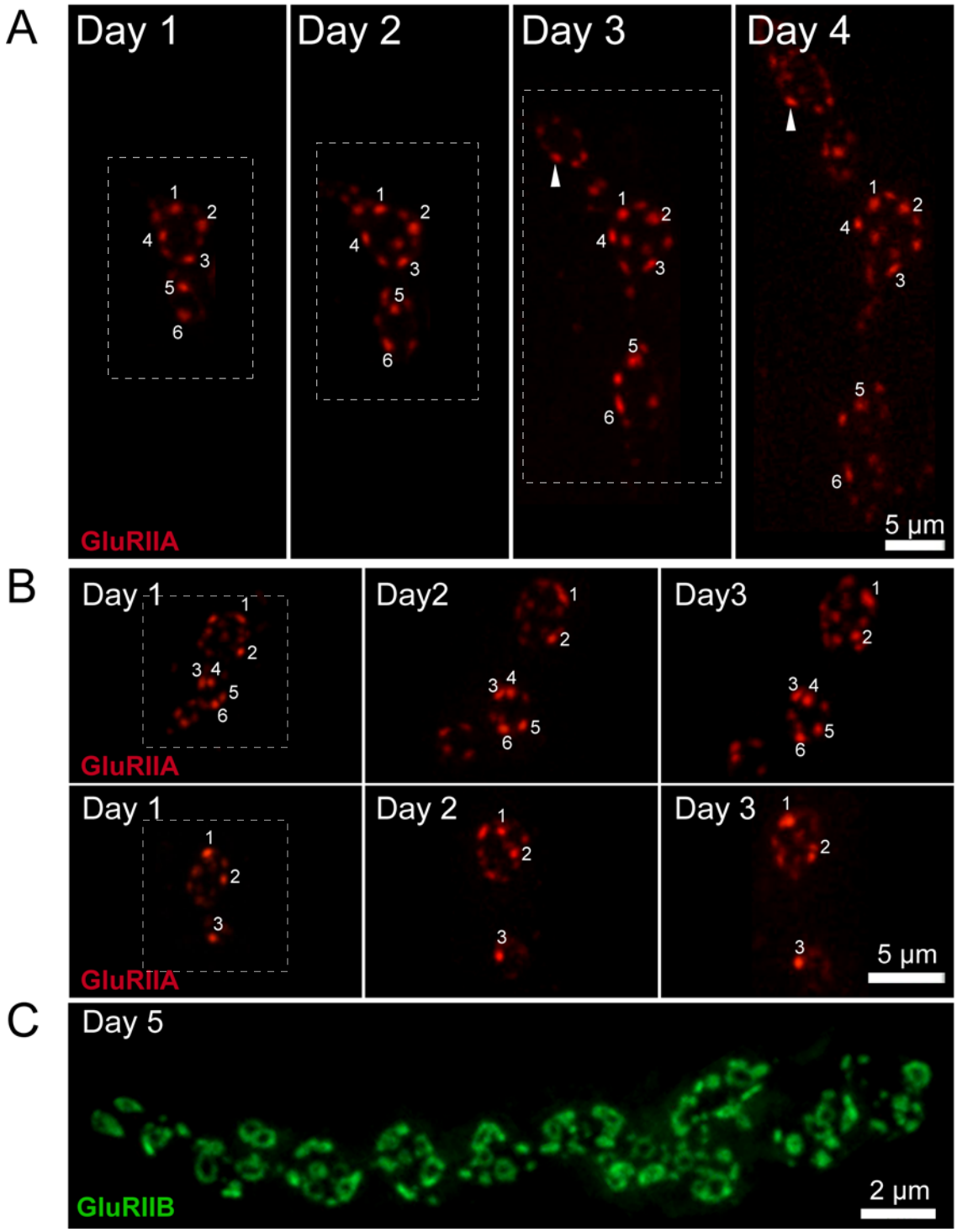

Figure 8 - figure supplement 3



A